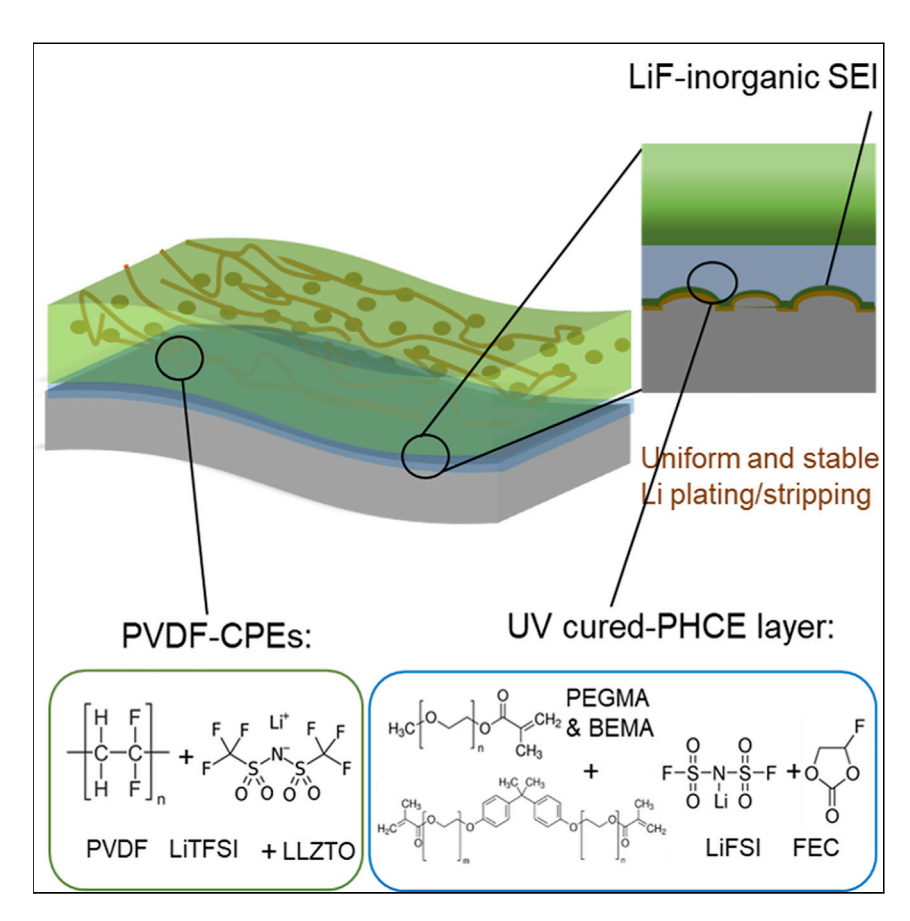


Article

In situ formation of polymer-inorganic solidelectrolyte interphase for stable polymeric solid-state lithium-metal batteries



Polymeric highly concentrated electrolyte on composite polymer electrolytes (PHCE-CPEs) enable both Li anode and high-energy Co-free LiNiO $_2$ cathodes to achieve high Coulombic efficiency of >99%, representing a new solution for polymeric solid-state batteries (SSBs). The design of PHCE-CPEs resolves the challenges from surface contact and dendrite penetration, while the principles can also be applied to other SSBs. These findings should therefore be of general interest to a broad audience working on batteries, material science and engineering, and electrochemistry.

Tao Deng, Longsheng Cao, Xinzi He, ..., Marshall A. Schroeder, Xiulin Fan, Chunsheng Wang

cswang@umd.edu

Highlights

Thin composite polymer electrolyte enables Li-metal batteries with Co-free LiNiO₂

No formation of dead Li with a Li plating/stripping efficiency of >99%

LiF-SEI and salt-rich interlayer suppress the formation of Li dendrites and dead Li

Highly reversible LiNiO₂ Li-metal battery with a retention of 81% after 200 cycles







Deng et al., Chem 7, 1–17 October 14, 2021 © 2021 Elsevier Inc. https://doi.org/10.1016/j.chempr.2021.06.019

Chem



Article

In situ formation of polymer-inorganic solid-electrolyte interphase for stable polymeric solid-state lithium-metal batteries

Tao Deng,^{1,4} Longsheng Cao,^{1,4} Xinzi He,^{1,4} Ai-Min Li,¹ Dan Li,¹ Jijian Xu,¹ Sufu Liu,¹ Panxing Bai,¹ Q1 Ting Jin,¹ Lin Ma,³ Marshall A. Schroeder,³ Xiulin Fan,¹ and Chunsheng Wang^{1,2,5,*}

SUMMARY

Composite polymer electrolytes (CPEs) for solid-state Li-metal batteries (SSLBs) still suffer from gradually increased interface resistance and unconstrained Li-dendrite growth. Herein, we addressed the challenges by designing a LiF-rich inorganic solid-electrolyte interphase (SEI) through introducing a fluoride-salt-concentrated Q8 interlayer on CPE film. The rigid and flexible CPE helps accommodate the volume change of electrodes, while the polymeric highly concentrated electrolyte (PHCE) surface-layer regulates Li-ion flux due to the formation of a stable LiF-rich SEI via anion reduction. The designed CPE-PHCE presents enhanced ionic conductivity and high oxidation stability of >5.0 V (versus Li/Li⁺). Furthermore, it dramatically reduces the interfacial resistance and achieves a high critical current density of 4.5 mA cm⁻². The SSLBs, fabricated with thin a CPE-PHCE membranes (<100 µm) and Co-free LiNiO₂ cathodes, exhibit exceptional electrochemical performance and long cycling stability. This approach of SEI design can also be applied Q2 to other types of batteries.

Q3 Q4 Q5 INTRODUCTION

Peyond Li-ion battery (LIB) technology, Li-metal batteries are reckoned as the most promising alternative to LIBs to meet the ever-increasing demand from electric vehicles and renewable energy market, such as solar, hydropower, wind, and other intermittent energy, due to the high theoretical specific capacity and lowest negative potential of Li-metal anodes (3,860 mAh g⁻¹, -3.04 V versus standard hydrogen electrodes). ¹⁻³ Among all, solid-state Li-metal batteries (SSLBs) using nonflammable inorganic or organic solid-state electrolytes (SSEs) have been explored mostly as the next-generation energy-storage devices. ^{4,5} The SSLBs are expected to not only provide high energy/power density but also eliminate safety concerns due to the replacement of highly flammable organic solvents.

To realize such a goal, a large number of SSEs with fast Li-ion conductivity have been investigated in the last several decades, such as sulfide-based glass/ceramic, garnet-type conductors, garnet-type conductors, long polymer-based electrolytes, long electrolytes, long electrolytes, long electrolytes, long electrolytes are soft and flexible, thus relieving the interface problems caused by stress/strain change in cycling. In polymer electrolytes, lithium bis(trifluoromethanesulfonyl) limide (LiTFSI) in polyethylene glycol (PEO)- or polyvinylidene fluoride (PVDF)-based composite polymer electrolytes (CPEs) have been studied mostly owing to their relatively high mechanical strength, good membrane-forming

The bigger picture

Next-generation rechargeable batteries, consisting of Li anodes, solid-state electrolytes, and Nirich cathodes, are desired to meet future energy-storage needs with high energy density, low cost, and safety. Developing composite polymer electrolytes (CPEs) is one of the right directions for achieving this goal. Extensive research has been devoted to exploring polymeric Li-metal batteries, but only limited progress has been made because of unstable interfaces and unconstrained Li-dendrite growth. Herein, we designed a thin saltconcentrated interlayer on CPEs via simple UV polymerization for stabilizing Li anodes and Co-free LiNiO₂ cathodes to achieve excellent cycling stability (81% retention after 200 cycles), rate performance, and high average Coulombic efficiency of >99.8%. This work provides a reliable method to make CPEs suitable for high-energy Li-metal batteries and thus paves the way to commercialization of quasi-solidor solid-state lithium batteries.





capability, as well as their excellent flexibility. $^{15-20}$ However, nearly all the polymer electrolytes show limited Li $^+$ conductivity, instability to Li anodes, and narrow electrochemical window (< 4 V), which has restricted their use in high-energy Li-metal batteries with high-voltage cathode. $^{12-15,17,21}$

Recent studies show that the symmetric Li cells based on the newly developed CPE films can only cycle at $0.2-0.5~\text{mA}~\text{cm}^{-2}$ for a limited period of time (Table S1), which is much worse than the cells with inorganic SSEs. ^{22–24} What is more, similar to inorganic SSEs, most of CPEs are always suffering from severe Li -dendrite penetration, dead-lithium formation, as well as continual increase of interface resistance due to unstable interphase formation (Figure 1A), thus making it difficult to develop practical polymeric batteries with high energy density and safety. ^{22,25–29} New surface strategies aiming to improve stability of electrode-electrolyte interfaces are needed to make thin CPEs compatible with a high-voltage cathode and a Li-metal anode if a polymer-based battery is to meet the energy-density specification >300 Wh kg⁻¹. The most recent results on high concentrated electrolytes (HCEs) show the Coulombic efficiency (CE) of Li plating/stripping can be increased to >99.6%, while the electrochemical window can be up to 5.0 V (versus Li/Li⁺), due to the formation of LiF-rich protective nanolayer on both cathode and Li-metal anode by solvent or Li salts reduction. ^{25,30–32}

Despite these advantages, HCEs seem inapplicable due to their high viscosity, worse wettability to the separator, as well as the high cost of Li salts. On the contrary, incorporating the chemistry of HCEs with the CPEs provides a good option to realize high-energy Li-metal batteries. Toward this end, we proposed to build a Li-salt-rich cross-linked polymer interlayer via one-step ultraviolet (UV) curing process on both sides of CPEs to stabilize Li anode and high-voltage Ni-rich cathode. As shown in Figure 1B, the newly designed PVDF-based CPE film with UV-polymerized HCE (PHCE) soft layer made of poly (ethylene glycol)methyl ether methacrylate (PEGMA) polymer and HCEs. The PVDF-based CPE film was selected due to its demonstrated excellent flexibility and mechanical strength. Meanwhile, the introduced UV-polymerized HCE layer can: (1) stabilize the Li anode by forming stable inorganic-rich solid-electrolyte interphase (SEI) and holding the morphological change as the buffering layer and (2) fabricate Ni-rich composite cathodes with the capability to limit the surface degradation. This rationally designed SEI, based on UV polymerization of HCEs, can also applied to other types of batteries.

RESULTS AND DISCUSSION

Characterizations of CPE and CPE-PHCE films

The CPE film acting as the main matrix electrolyte layer was prepared using a previously reported solution-casting method with the slurry containing PVDF polymer, LiTFSI and Li $_{6.5}$ La $_{3}$ Zr $_{1.5}$ Ta $_{0.5}$ O $_{12}$ (LLZTO) filler. 16,33 The thickness of CPEs was optimized to be \sim 70 μ m to achieve the high energy density of Li-metal batteries. As shown in the inset of Figure S1A, the vacuum-dry CPEs with LLZTO filler present a yellowish color due to the interactions between cationic functionalities and solvent molecules near the surface of LLZTO filler, which were believed to improve the ionic conductivity of CPEs. 33 The addition of inorganic filler is to increase the strength of CPEs, as well as the Li $^+$ ionic conductivity and transference number. 34,35 Figures S1A and S1B show scanning electron microscope (SEM) images of the top surfaces of PVDF-based CPEs, which present porous structures and granular surfaces. Such porous surface structure might cause large interfacial resistance and non-homogeneous Li dissolution/deposition in cycling. The energy-dispersive X-ray

¹Department of Chemical and Biomolecular Engineering, University of Maryland, College Park, MD 20742, USA

²Department of Chemistry and Biochemistry, University of Maryland, College Park, MD 20742, IISA

³U.S. Army Combat Capabilities Development Command, Army Research Laboratory, Energy and Biotechnology Division, Adelphi, MD 20783, IISA

⁴These authors contributed equally

⁵Lead contact

^{*}Correspondence: cswang@umd.edu https://doi.org/10.1016/j.chempr.2021.06.019





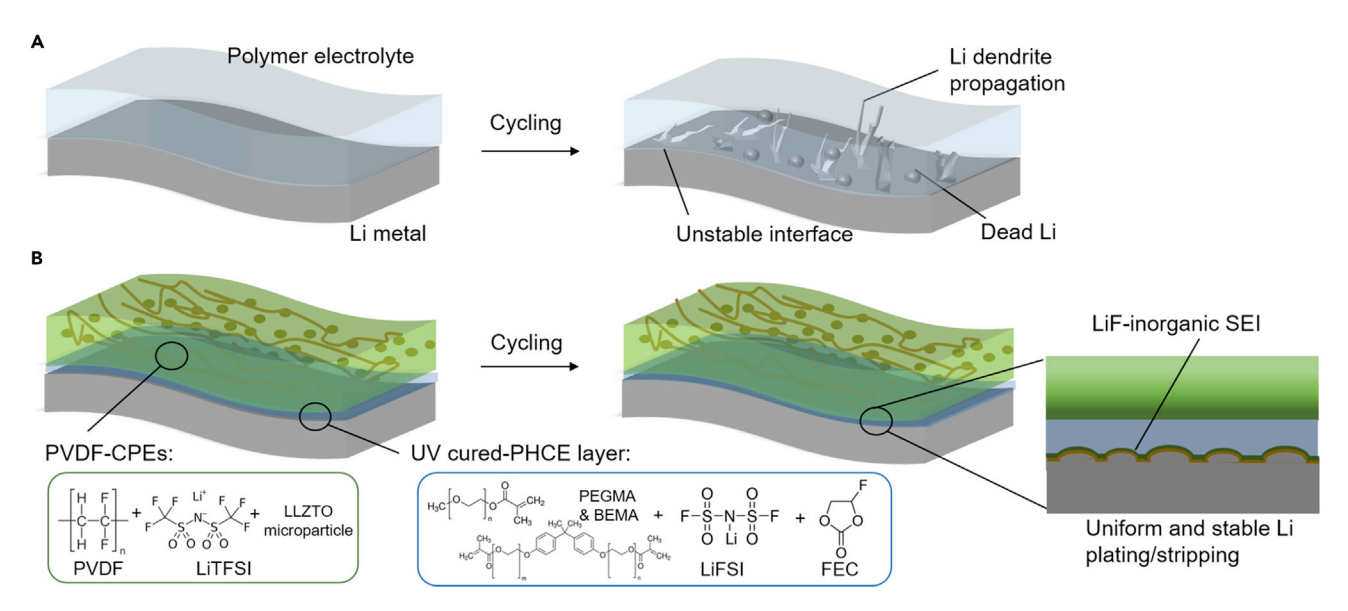


Figure 1. Illustration of the interface design of inorganic-rich SEI using UV-cured PHCE thin layer

(A) Typical polymer electrolytes cannot form stable SEI with Li metal, leading to dead-Li accumulation and Li-dendrite propagation in cycling. (B) Rational design of LiF-rich inorganic SEI via decomposition of UV-cured PHCE layer with a thickness of \sim 6 μ m. The attachment of the PHCE layer enhances the surface homogeneity of CPEs and passivates the Li surface by generating an LiF-rich SEI layer with inorganic anion-derived components (brown). The unreacted PHCE layer (blue) acts as a buffering layer to regulate the Li deposition and relief the stress due to morphology change, thus realizing stable and dendrite-free Li cycling.

spectroscopy (EDS) of the CPEs presents uniform distribution of Zr, N, O, and S compounds, confirming the distribution of microsized garnet-type solid-electrolytes filler and LiTFSI salt on the surface (Figures S1C–S1F).

CPE film and HCEs with different salt concentrations were characterized using Raman spectra to demonstrate the Li-ion solvation structure within the PHCE top layer. In Figure 2A, an upshift of the bis(fluorosulfonyl)imide (FSI) band (from 720 to 732, and 744 or 759 cm⁻¹) indicates the coordinated structure of Li⁺-FSI⁻-solvent clusters, and the low proportion of free fluoroethylene carbonate (FEC) molecules is presented at highly concentrated samples—e.g., CIP (contact ion pairs) and AGG (aggregates). These results appear comparable with those from previously reported concentrated aqueous electrolytes. ^{21,36} Compared with the Raman spectra of HCEs and precursor solution, UV-polymerized HCE film (PHCE) presents a reduction of Q9 AGG cluster (to 744 from 759 cm⁻¹) due to the dissociation and incorporation effects of PEGMA polymer, which indicates a higher Li-ion conductivity of UV-polymerized HCEs (PHCE) than the utilized HCEs.

Figure 1B shows the X-ray diffraction patterns (XRD) of prepared CPE with PHCE (CPE-PHCE), CPEs, lithium bis(fluorosulfonyl)imide (LiFSI), and PVDF powder, as well as the pure-PEGMA gel layer after UV polymerization. Although the UV-cured PEGMA layer has a relatively strong crystalline peak at around 20°, the addition of LiFSI-FEC makes the peak of CPE-PHCE significantly broader at the same position. It suggests that the plasticization of LiFSI-FEC can destroy the PEGMA's hard-segments crystal, thereby reducing the crystallinity of polymer electrolyte system. ³⁷ In addition, the diffraction peaks at $2\theta = 17.8^{\circ}$, 18.4° , 19.9° , and 26.6° are attributed to the (100), (020), (110), and (021) planes of a typical α-PVDF crystal structure, respectively (Figure S2). ³⁸ The weakening and shifting of these peaks indicates the PVDF transformation from α-phase to γ-phase due to decreased crystallinity, which



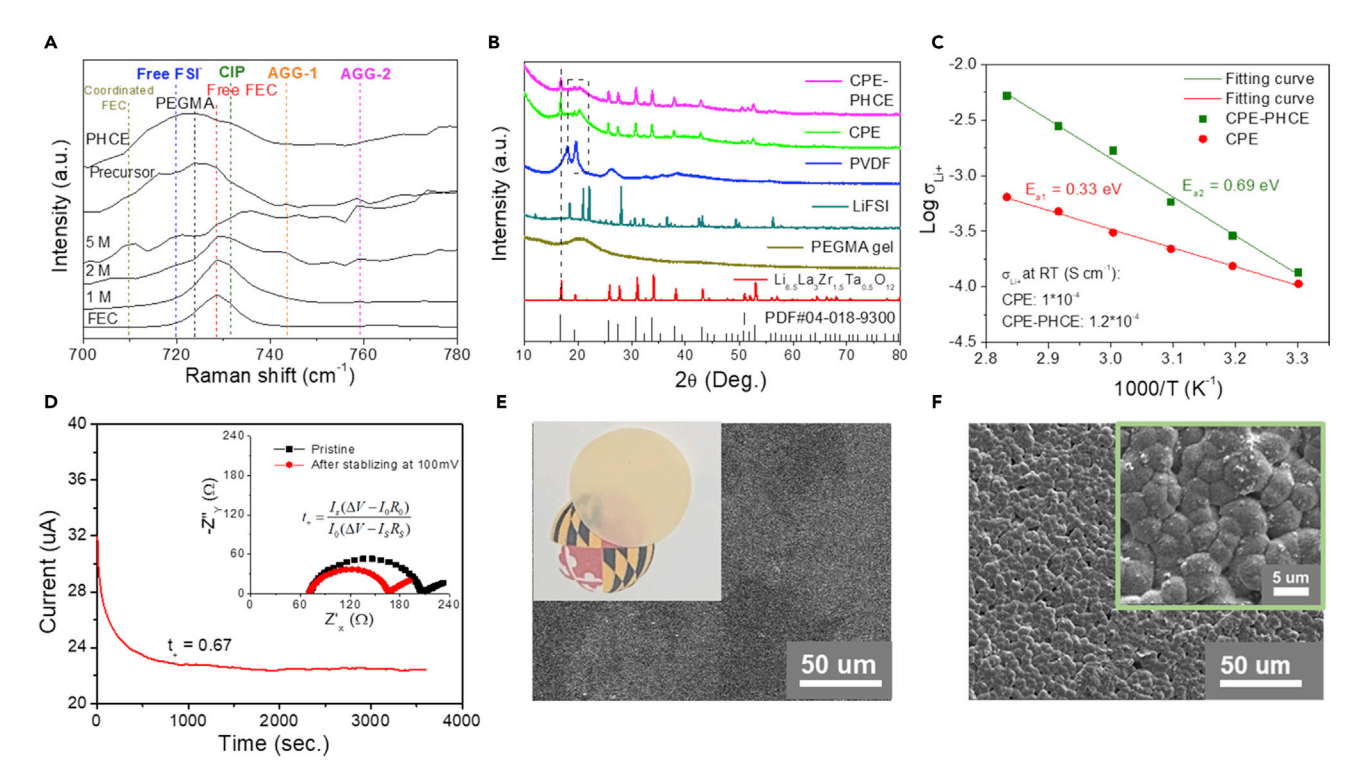


Figure 2. Physical characterization of the CPE and PHCE electrolytes

- (A) Raman spectra of various concentrations of LiFSI-FEC electrolytes, precursor solution, and UV-curved PHCE showing the change of Li⁺ solvation structure.
- (B) XRD patterns of LLZTO, PEGMA gel, LiFSI, PVDF, CPE, and CPE-PHCE.
- (C) Arrhenius plot of CPE and CPE-PHCE electrolytes at temperatures from 30°C to 80°C.
- (D) Current-time profile of Li|CPE-PHCE|Li symmetric cell after applying a DC voltage of 100 mV for determining Li⁺ transference number. The inset shows the Nyquist impedance spectra of the cell before and after polarization.
- (E) SEM image of the top view of CPE-PHCE film, the inset shows digital image of thin yellowish CPE-PHCE film.
- (F) SEM images of top surface of the PVDF-based CPE film, which presents a nonhomogeneous surface with porous structure and dispersed LLZTO particles.

is believed to enhance the Li-ion conductivity of CPE film. ^{16,33,39-41} Overall, the amorphous structure of polymer was reported to facilitate intra- or interchain hopping, which relates with the movement of segmental polymer chains with sequential coordinated sites to Li ions, thus increasing the Li⁺ ionic conductivity of the electrolyte. ^{12,42}

Li⁺ ionic conductivities of the CPE and CPE-PHCE film electrolytes at temperatures ranging from 30°C to 80°C are plotted in Figures 1C and S3. As can be seen, the Li⁺ ionic conductivity of CPE-PHCE membrane increases to 1.2 × 10^{-4} S cm⁻¹ at RT (versus 1.0 × 10^{-4} S cm⁻¹ for CPEs) due to the coating of high-salt layer. The increase of curve slope indicates the change of Li-ion transport mechanism at high temperature due to the dissociation of Li salts. The calculated activation energies are 0.33 and 0.69 eV for CPE and CPE-PHCE, respectively, which indicate CPE-PHCE is more temperature-dependent since high temperature facilitates the Li-ion dissociation of HCE and Li⁺-chain hopping within CPE-PHCE. In addition, the CPE-PHCE and CPEs also present Li-ion transference numbers (t₊) as high as 0.67 and 0.63, respectively (Figures 1D and S4), which is much larger than the reported 0.22 for regular 1.0 M LiPF₆-ethylene carbonate/diethyl carbonate (EC/DEC = 1:1, by volume).³⁵ The high t₊ of CPE-PHCEs represents the highly efficient Li-ion

Please cite this article in press as: Deng et al., In situ formation of polymer-inorganic solid-electrolyte interphase for stable polymeric solid-state lithium-metal batteries, Chem (2021), https://doi.org/10.1016/j.chempr.2021.06.019





transport across the membrane, thus reducing the dendrite formation under high current density by weakening the space charge near Li metal.^{22,28}

We further investigated the thermal stability of PVDF-based CPE-PHCE membrane with a thermogravimetric analyzer (TGA). As indicated in Figure S5, the thermal degradation of pure PVDF starts at around 420°C, and the thermal stability of CPE-PHCE is worse than CPE due to the PHCE layer. The weight loss of the CPE and CPE-PHCE membranes starting before 200°C might be related to the evaporation of moisture or trapped dimethylformamide (DMF) or FEC of PHCE layer, and the loss before 330°C corresponds to the polymer melting and gradual degradation of Li salts, affected by the interactions between LLZTO, polymer matrix, and lithium salts. Furthermore, the weight loss of CPE-PHCEs began at 160°C, which should be good enough to be applied in lithium-metal batteries operated at intermediate temperatures. The inset of Figure 1E shows the digital image of a thin CPE-PHCE film as the separator of SSLBs. Compared with the porous and nonhomogeneous CPE surface (Figure 1F), the UV-cured PHCE layer presents a flat and uniform surface, thus improving the contact with Li anode and composite cathodes.

Structure and composition distribution of CPE-PHCE film

The molecular structure of the PHCE thin layers fabricated via UV curing was examined by Fourier transform infrared spectrometer (FTIR) and nuclear magnetic resonance (NMR). As shown in Figure S6A, the disappearance of C=C functional group (1,635 cm⁻¹) in the FTIR spectrum of PHCE layers demonstrates the successful polymerization of PEGMA with cross-linker bisphenol A ethoxylate dimethacrylate (BEMA). The signals of carbonyl (C=O, 1,461, 1,722 cm⁻¹) and C-O-C groups (1,102 cm⁻¹) in polymer backbone remain unchanged, and thus, these functional groups will help the Li⁺ dissociation and transport. In addition, the FTIR spectrum of PHCE layer also presents the same peak for FEC (1,800 cm⁻¹) as 12M LiFSI-FEC electrolyte, which indicates the UV-curing process has no influence on the LiFSI-FEC solvation structure and no side reactions happen during polymerization. The NMR spectra in Figure S6B shows two peaks (6.0 and 5.7 ppm) related to the hydrogen atoms connected to C=C bonds in PEGMA. After UV curing, these two peaks disappear, while the LiFSI-FEC peaks (Figures S6B and S7) present in the NMR spectrum of PHCE layer. Therefore, both FTIR and NMR results indicate that the UV-curing polymerization happens for PEGMA-BEMA, while LiFSI-FEC remains in the polymer backbone.

To unveil the underlying mechanism of lithium-dendrite suppression for the designed CPE-PHCE membrane, it is essential to know the structure and material distribution across the surface of the electrolyte. Figure 3A shows the SEM image of the cross-section of CPE-PHCE film, which presents a flat and uniform surface with a thickness of $\sim 80~\mu m$. The flat ($\sim 6~\mu m$) and soft PHCE layer enhances surface homogeneity of film electrolytes and helps keep good contact with the Li anode, thus leading to uniform Li deposition/dissolution near the interface. We further characterized the CPE-PHCEs with time of flight secondary ion mass spectrometry (ToF-SIMS) via the sputtering of Ga⁺ ions (Figures 3B and 3C). In the depth range of $\sim 5~\mu m$, the CPE-PHCE membrane presents a salt-rich layer by presenting extremely highly concentrated F, S, Li, and O elements due to the good incorporation of HCEs.

The atomic force microscope (AFM) can simultaneously map the roughness and mechanical properties of the extrinsic interface with nanoscale resolution. 43,44 In Figures 3D and S8A, the 2D AFM topography images based on scanning probe spectroscopic method show the average roughness (R_a) is around 52 and 420 nm for



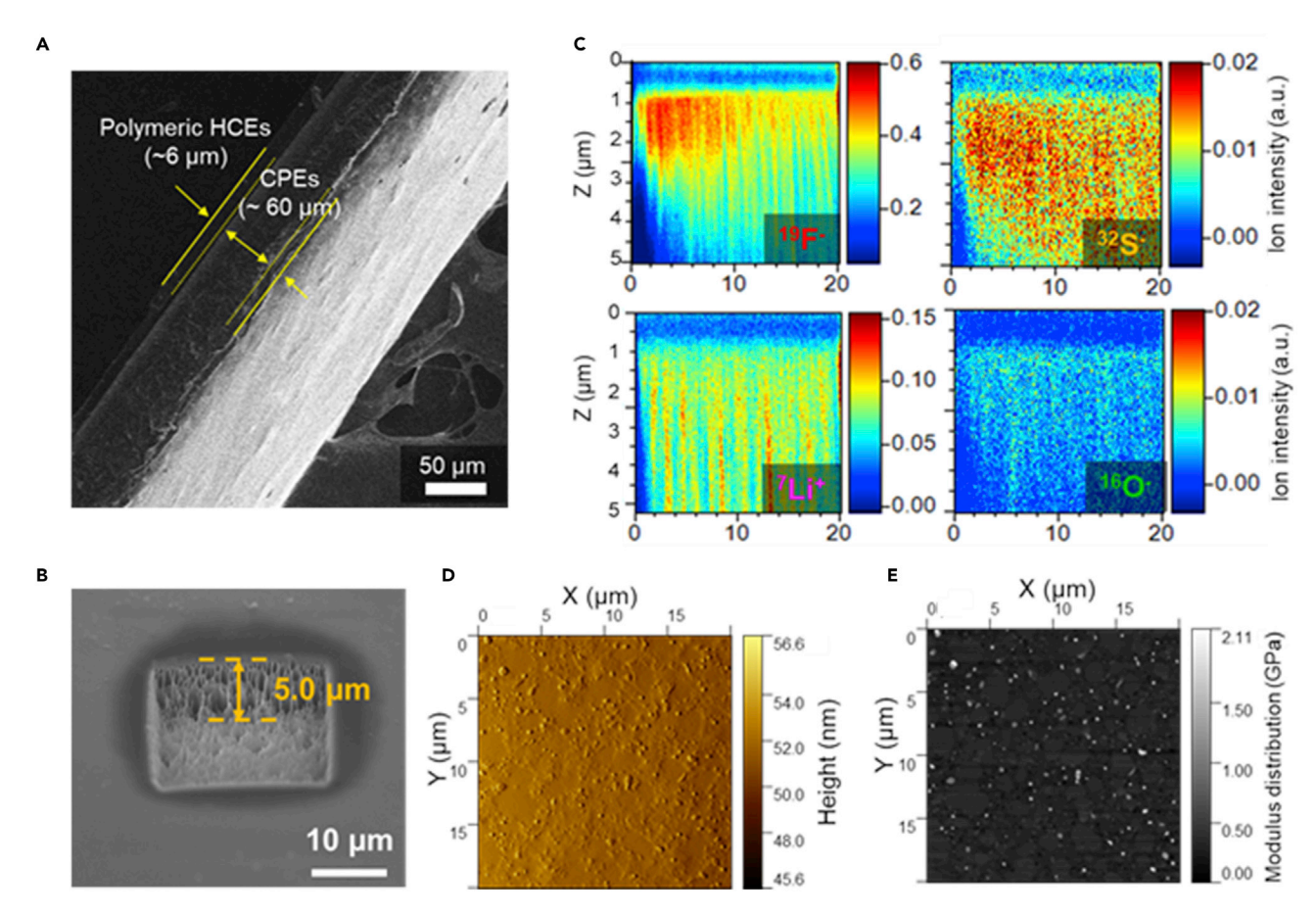


Figure 3. Structure and composition profiles of CPE-PHCE electrolytes

- (A) SEM image of the cross-section of CPE-PHCE film, which presents double-layered structure with a layer of PHCE on the top.
- (B) Surface morphology of top layer for ToF-SIMS and the crater is sputtered by Ga^+ ion beam.
- (C) The depth profiles of ToF-SIMS analysis for $^{19}F^-$, $^{32}S^-$, $^7Li^+$, and $^{16}O^-$ species, demonstrating the existence of high-salt layer with a thickness of $\sim 5~\mu m$.
- (D) AFM images (20 μm × 20 μm) of CPE-PHCE film with small surface roughness ($\sim\!50$ nm).
- (E) AFM mapping of the effective Young's modulus of CPE-PHCE film.

CPE-PHCEs and CPEs, respectively. The micropores and rough surface of CPE film (Figure 2F) can be attributed the aggregation of LLZTO particles on the surface, as well as the reduction of plasticizers and amorphous phases after vacuum heating. Mechanical properties are quantitatively described by the Young's modulus obtained from force indentation curves (Figures 3E and S8B). Since the Young's modulus of polymer film is highly dependent on the material distribution on the surface, the flat CPE-PHCE film shows a uniform modulus distribution (~0.5 GPa), confirming homogeneous morphological and mechanical properties of the CPE-PHCE film. The small white spots with high modulus (~2.0 GPa) in Figure 3E might be caused by the LLZTO particles beneath the thin PHCE layers.

Li plating/stripping stability and dendrite suppression capability of CPE-PHCE

To demonstrate the electrochemical performance of the CPE-PHCE film electrolytes, Li|CPE-PHCE|SS (stainless steel) cells were prepared to determine the oxidation limit and Li-anodic stability via cyclic voltammetry (CV) (Figure 4A). Compared with CPE film electrolyte (Figure S9A), the good overlapping of curves from -0.5 to 2.0 V shows the excellent cycling stability of CPE-PHCE with lithium due to the





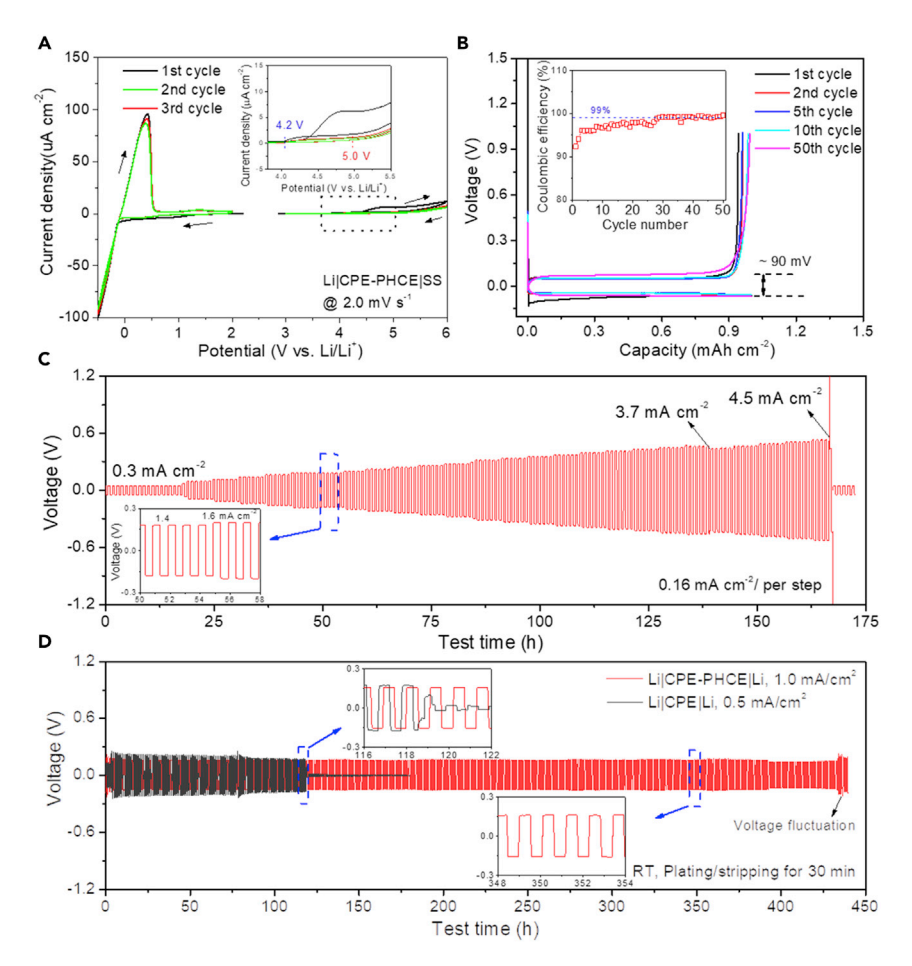


Figure 4. Electrochemical characterization of the CPE-PHCE electrolytes at RT

(A) Cyclic voltammetry curve of Li|CPE-PHCE|SS cell from -0.5 to 2.0 and 3.0 to 6.0 V, showing CPE-PHCEs have excellent stability to Li metal and good oxidation stability up to 5.0 V after forming a passivation layer.

(B) Li-metal plating/stripping profiles of Li|CPE-PHCE|Cu cell at a current density of 0.5 mA cm $^{-2}$ with areal capacity of 1.0 mAh cm $^{-2}$, and the inset shows the change of Li plating/stripping Coulombic efficiency.

(C) Voltage profiles of the cell under step-increased current densities from 0.3 to 4.5 mA cm $^{-2}$ for 30/30 min of Li plating/stripping time (\sim 0.16 mA cm $^{-2}$ per step).

(D) Comparison of DC cycling for Li symmetric cells of Li|CPE-PHCE|Li and Li|CPE-PHCE|Li at current densities of 1.0 and 0.5 mA cm^{-2} , respectively with plating/stripping time of 30 min.

existence of a polymeric HCE layer. On the other hand, the curves between 3.0 and 6.0 V indicate that a passivation process existing on the SS|CPE-PHCE interface at around 4.2 V. Once the stable passivation layer is formed at the first cycle, the oxidation stability of CPE-PHCEs can be enhanced to 5.0 V, which is much larger than that of CPEs (3.9 V) (Figure S9B). In addition to CV, the lithium plating/stripping CE with the CPE-PHCEs was also demonstrated using a Li-free configuration coin cell (Li|CPE-PHCE|Cu) (Figure 4B). At a current density of 0.5 mA cm⁻², the Li plating/stripping CE of Li|CPE-PHCE|Cu cell increases to >99% in 30 cycles with a small polarization of 90 mV after stabilization, while for CPE film electrolytes, the cell quickly 210 short circuited in 15 cycles with an average CE of 95% and large polarization of 120 mV (Figure S10). Thus, remarkable cycling stability and stable Li plating/stripping potential can be achieved by the designed CPE-PHCEs.





Critical current density (CCD) measurement was conducted to demonstrate the capability of CPE-PHCEs to suppress Li-dendrite penetration using the Li symmetric cell under fixed Li plating/stripping time of 30 min for 6 cycles with step-increased current density (0.16 mA cm⁻²/per step). As shown in Figure 4C, the cycling of cell is quite stable and its potential response closely follows Ohm's law under different current densities. The voltage is around 50 mV at 0.3 mA cm^{-2} due to the enhancement of bulk ionic conduction and surface contact. When the current density increased to 3.7 mA cm⁻², the corresponding voltages drop from 0.46 to 0.44 V, indicating the invading of deposited Li into the PHCE layer under high current density, thus reducing the polarization. Finally, the cell was totally short circuited by Li dendrites when the current reached to a record-breaking value of 4.5 mA cm⁻² with a high capacity of 2.25 mAh cm⁻², which have never been reported for polymer-based electrolytes. Furthermore, the enlarged views showing the stable polar-Q11 ization under different currencies confirms that the designed CPE-PHCEs are able to hold the dimensional change of Li anode even under high areal capacity of >2.0 mAh cm^{-2} .

The long cycling stability of CPE-PHCE film electrolyte was further demonstrated with the Li symmetric cells under high current density/high areal capacity (1.0 mA cm⁻² and 0.5 mAh cm⁻², respectively). As can be seen in Figure 4D, the cell presents small and stable voltages (~160 mV) even after more than 400 h of cycling. On the contrary, the Li symmetric cell with CPE membrane shows large polarization (\sim 180 mV) with potential fluctuation when cycled at 0.5 mA cm $^{-2}$. The uneven Li dissolution/deposition caused by unstable interphase formation leads to Li-dendrite formation and finally shorts the cell at 118.2 h due to dendrite penetration. The Li symmetric cells using polymer electrolytes display miner "arc" voltage curves, which highly correlate to the high softness of the polymer and good surface contact (Figures 4C, 4D, and S11). As shown in Figure S11A, the voltage polarization during Li plating at different current densities for the Li symmetric cells with CPE-PHCE film is small (<0.03V) due to the formation of stable SEI and surface contact enhancement by the homogeneous PHCE layer. However, the Li symmetric cell with CPE film shows a large polarization of 0.25 V at 0.5 mA cm⁻², which is caused by the nonhomogeneous surface of CPE. The voltage and polarization were continually reduced with the cycling and reached 0.17 V at 109.1 h before short circuit occurred (Figure \$11B). Such decreases of cell voltage might be related to dead-Li accumulation near the Li/CPE interface or Li propagation along the CPE film.

Meanwhile, the polymeric HCEs with glass fiber support (Figure S12A) was prepared to demonstrate the necessity of the CPE-PHCE design. It should be noted that the PHCE-glass fiber film is brittle and would crack under high stacking pressure (Figure S12B). As shown in Figures S12C and S12D, the Li symmetric Li|PHCE-fiber|Li Swagelok cell has low cell resistance and is able to stably cycle for more than 450 h at 0.4 mA cm⁻² without short circuiting. In our study, the design of CPE-PHCE is necessary to provide enough mechanical strength and flexibility to prevent Li-dendrite propagation after long cycling. Overall, stable Li platting and stripping with low polarization can be achieved with our newly designed CPE-PHCE film electrolyte.

Interface chemistry of CPE and CPE-PHCEs

Generally, since most polymers are chemically unstable to Li-metal and cannot form stable SEI through self-passivation process, the unstable Li plating/stripping induced by chemical or mechanical nonhomogeneity of CPE can easily form Li dendrites and penetrate the membrane in a short time (Figure 5).^{21,43,44} In the case of



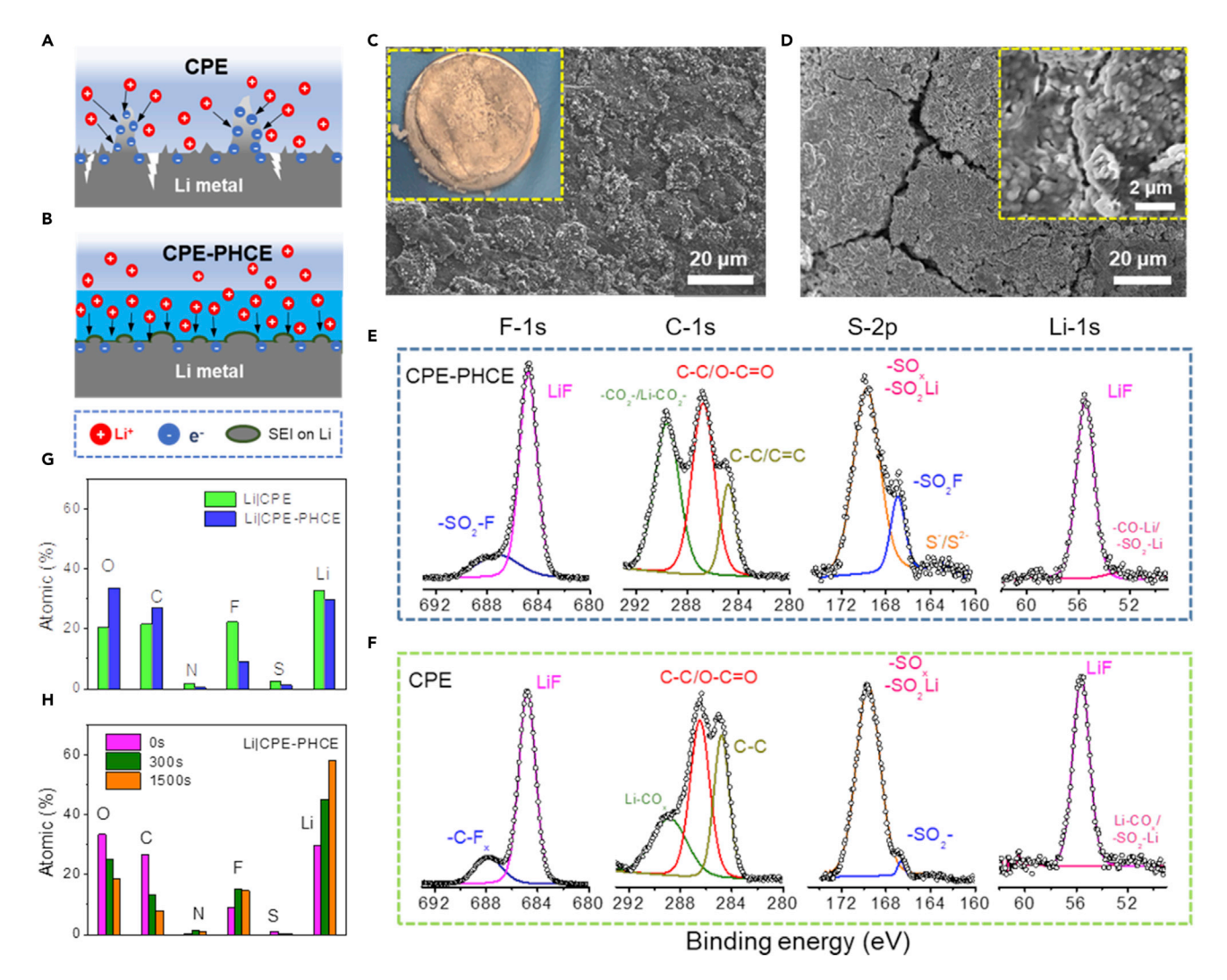


Figure 5. Interface chemistry of CPE-PHCE and CPE electrolytes

- (A) Schematics of lithium-dendrite propagation penetrating CPE film due to surface nonhomogeneity and unstable SEI formation.
- (B) Proposed mechanism of polymer-inorganic SEI and HCE layer for regulating Li dissolution/deposition to achieve dendrite-free Li cycling.
- (C) SEM image of cycled Li-metal with CPE-PHCE and the inset shows digital picture of clean surface without dead Li.
- (D) SEM image of cycled Li metal with CPE and its surface was covered with recrystallized Li particles with crack formation due to surface inhomogeneity. (E and F) XPS spectra of F-1s, C-1s, S-2p, and Li-1s for cycled Li metal with (E) CPE-PHCE and (F) CPE.
- (G) Comparison of elemental concentration on SEI of cycled Li metals.
- (H) XPS elemental concentration of the SEI on cycled Li metal with CPE-PHCE after Ar sputtering of 0, 300, and 1,500 s. The cycled Li metals were obtained from symmetric Li|CPE-PHCE|Li and Li|CPE|Li cells after cycling at 0.5 mA cm⁻² for 50 h at RT.

CPE-PHCE, the PHCEs from UV polymerization enables uniform concentration gradients and the formation of stable SEI near the Li|CPE-PHCE interface, thus realizing uniform Li⁺ deposition/dissolution by minimizing transport limitations and local degradation (Figure 5B). Figures 5C and 5D show the SEM morphology of cycled Li metals on CPE-PHCE and CPE films. The surface of cycled Li metal on CPE-PHCEs presents relatively dense and mound-like morphology due to recrystallization of Li in cycling, and no obvious Li dendrites were formed during the prolonged cycling at 0.5 mA cm⁻². The EDS mapping also indicates the formed SEI on Li metal is rich in C, F, N, O, and S compounds, originating from the reduction of Li salts and polymers (Figure S13). The formed SEI film prevents the Li-dendrite penetration even





under high current densities (\sim 4.5 mA cm $^{-2}$). As for the cycled Li metal with CPE membrane, the surface presents uneven surface morphology with some large surface cracks due to the nonuniform Li plating/stripping (Figure 5D). The uneven surface tends to further worsen the contact between CPE membrane and Li metal, leading to an increase in cell polarization and formation of dead lithium (Figure S14). The formation of dead lithium can be related to the nonuniform Li deposition/dissolution in cycling, originating from the surface nonhomogeneities of CPE, such as PVDF-membrane surface defects, random distribution of LLZTO, (Figure S1), etc.

We also observed the deposited Li particles on the surface defects of cycled CPEs (Figure S14), which might help explain the partial short circuit of CPE in long cycling. Figure S15A compares the XRD patterns of pristine CPEs with the shorted CPEs at 0.5 mA cm $^{-2}$. The picture of cycled CPE membrane (Figure S15A, inset) shows some dark yellowish areas due to the corrosion of reactive Li metal. In addition, the XRD pattern shows the coloration of CPEs results in the formation of Li₂CO₃ (200, 111, 002, and 020) and LiF compounds via PVDF decomposition, which was also accumulated on the top of cycled Li-metal in Figure S15B. What is more, the shorted region of CPE membrane shows irregular morphology with dead lithium attached on the top and CPEs (Figures S15B and S15C). These results illustrate the necessity of forming a stable SEI for the Li/CPE interface to achieve uniform Li dissolution and deposition.

To identify the chemistry at the interface, we performed high-resolution X-ray photo-electron spectroscopy (XPS) and elemental concentration analysis on the cycled Li metal. As schematically illustrated in Figure 5B, the top surface of the Li metal should be covered by the unreacted UV-cured HCE layer, and the SEI resides between this unreacted HCE layer and Li. After comparing the component differences in Figures 5E and 5F, we found the SEI on Li|CPE-PHCE interface contains significant high content of LiF (684.8 and 55.6 eV for F-1s and Li-1s, respectively) with organic compounds (–CO₂-/-Li-CO₂-, 289.6 eV) and unreacted FSI anions (687.2, 167.2, and 169.7 eV in the F-1s and S-2p spectra, respectively). What is more, the C and O atomic ratios for CPE-PHCE are 26.9% and 33.5%, respectively, which is slightly higher than those of the CPE sample (21.3% for C and 20.2% for O) (Figure 5G). These differences indicate distinct structure and chemical distribution of SEI formation for CPE-PHCE and CPE membranes.

We further characterized the composition profiles of SEI by sputtering the cycled Li Q12 metal with different times for knowing the SEI formation mechanism of CPE-PHCE and CPE membranes. Figure \$16 shows the XPS spectra of cycled Li-metal with CPE-PHCE after sputtering for 0, 300, and 1,500 s. In the depth profile of F-1s and C-1s, we observed an increased intensity of LiF (684.8 eV) but a reduced density of organic compounds (-CO₂-/-Li-CO₂-, 289.6 eV; C-C/O-C=O, 286.8 eV). At the same time, the depth profile of S-2p presents a sharp increase in the intensity of peaks for S^{-}/S^{2-} (<164 eV), while the Li-1s depth profile shows an increased intensity of LiF (55.6 eV) and -C-O-Li/-SO₂-Li (52.7 eV). Collectively, the PHCE layer of CPE-PHCE induces the formation of SEI including FSI-derived inorganic (LiF)-rich inner layer and polymeric Li salts as the outer layer. While for the CPEs, the SEI on Li metal mainly consists of PVDF-derived components, such as LiF, Li₂CO₃, and reduced Q13 polymer. XPS elemental concentration analysis further supports our finding on the SEI formation (Figure 5B). The SEI of the Li|CPE-PHCE interface has a high content of C (26.9%) and O (33.5%) and a low content of Li (29.6%) and F (8.9%) before sputtering. After sputtering for 1,500 s, the SEI presents a much higher content of Li (58.2%) and F (14.8%), and a lower content of C (7.9%), O (18.6%) This is in clear Please cite this article in press as: Deng et al., *In situ* formation of polymer-inorganic solid-electrolyte interphase for stable polymeric solid-state lithium-metal batteries, Chem (2021), https://doi.org/10.1016/j.chempr.2021.06.019





contrast with the CPE-derived SEI, which has unchanged concentrations of O (15.9%) and F (22.8%) after sputtering (Figure S17).

Based on these results, we conclude that the designed CPE-PHCEs combining the chemistry of HCEs with CPEs are able to form an inorganic-rich inner SEI layer, thus realizing stable Li dissolution/deposition. For CPE membrane, the organic-inorganic mixed SEI mainly derived from PVDF decomposition has low interface energy against Li, which suppresses lateral Li⁺ flux along Li/SEI but promotes vertical Li-dendrite growth.²⁹ For the cell with CPE membrane, the continual reduction of polymer causes the volume change of polymer (Figure S15C), leading to the formation of a thick SEI layer with worse Li-ion conductive capability. Such SEIs are organic rich and have low interface energy against Li, which suppresses lateral Li⁺ flux along Li/SEI but promote vertical Li-dendrite growth.^{25,45} On the contrary, the SEI formed by the PHCE layer is relatively thin and rich in FSI-derived inorganics (LiF), which have excellent mechanical strength and chemical/electrochemical stability to Li metal (Table S2). Due to the high interface energy and much lower energy barrier for Li⁺ surface diffusion (0.17 eV for LiF and 0.23 eV for Li₂CO₃),^{46,47} the LiF-rich inorganic SEI promotes Li⁺ migration along the LiF surface, thus realizing stable and smooth Li deposition/dissolution and preventing Li-dendrite penetration. ^{25,32} What is more, the PHCE layer from UV polymerization enables uniform Li⁺ concentration gradients and mechanical distribution near the Li|PHCE interface, which also helps eliminate the irregular Li growth when Li plating. As a result, the good contact between PHCEs and Li metal is kept even after cycling at 1.0 mA cm⁻² for more than 400 h.

Li/LiNiO₂ full cells with CPE and CPE-PHCEs

The thin and flexible polymer electrolytes are key to enabling high-energy, foldable batteries for next-generation flexible electronics and devices. The inset of Figure 6A shows a schematic of a flexible high-energy-density Li-metal battery coupled with a high-capacity lithium anode and a high-energy Ni-rich LiNiO₂ cathode (LNO). The LNO composite cathode with good Li⁺ conductivity capability was prepared by diffusing the precursor solution into LiNiO₂ cathode made from the solution-casting method, then followed by rapid UV polymerization (Figure S18A). Thanks to the soft and good flexibility of HCE layer, the LNO composite cathode can be closely attached on the CPE-PHCE membrane (Figure S18B). Nyquist plot from electrochemical impedance spectroscopy (EIS) of the prepared Li|CPE-PHCE|LNO cell indicates the total resistance of the cell is around 570 Ω cm², while the bulk resistance (RCPE + RHCE) reaches 400 Ω cm² (Figure 6A). The interface resistance and kinetics of Li-ion transferring within LNO cathode can be improved by optimizing the components and thickness of CPE-PHCE membrane.

Figure 6B shows charging/discharging curves of the Li|CPE-PHCE|LNO cell with an areal capacity of 0.8 mAh cm $^{-2}$ between 2.7 and 4.4 V. Under a constant current of 0.5 C (1 C = 200 mA g $^{-1}$), the cell presents a stable capacity of $\sim\!200$ mAh g $^{-1}$, which corresponds to 74% of the theoretical capacity (270 mAh g $^{-1}$). The slight increase of capacity at the initial cycling is due to the enhanced conductivity by breaking the surface film on cathode particles in cycling. The high Coulombic efficiency after the first formation cycle ($\sim\!99.9\%$) and small polarization increase proved that the PHCE has good stability to Ni-rich cathodes by forming stable cathode-electrolyte interphase (CEI) (Figure S19). In addition, the LNO cell based on designed CPE-PHCE membrane also presents excellent rate capability when charged/discharged with different C-rates ranging from 0.1 to 4.0 C (Figures 6B and 6C). As can be seen, the cell can deliver high capacities of 245, 221, 200, 154, 141, and 122 mAh g $^{-1}$



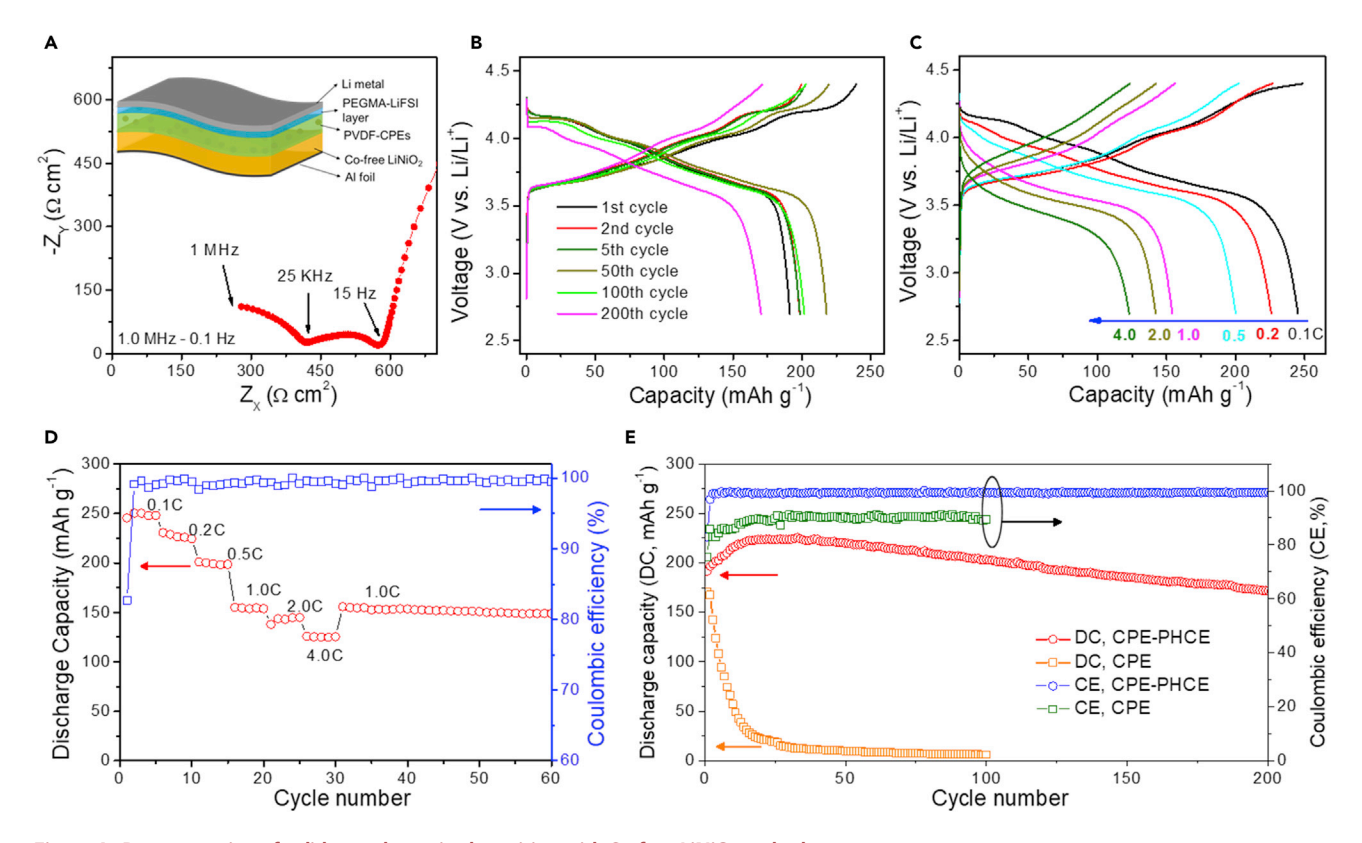


Figure 6. Demonstration of solid-state batteries by pairing with Co-free LiNiO_2 cathode

- (A) Typical Nyquist plot of Li|CPE-PHCE|LNO cell; the inset shows the schematics of high-energy Li-metal battery based on LNO composite cathode and designed CPE-PHCE film.
- (B) Charging/discharging curves of Li|CPE-PHCE|LNO cell at 0.5 C (0.4 mA cm⁻²).
- (C) Charge/discharge curves of Li|CPE-PHCE|LNO cell at different C-rates from 0.1 to 4.0 C.
- (D) Rate capability of the LNO cell at different current densities, increasing from 0.1 C to 4.0 C.
- (E) Corresponding cycling stability of the LNO cells with CPE and CPE-PHCE at 0.5 C. (1C = 200 mA g^{-1} ; the areal capacity of composite cathode is $\sim 0.8 \text{ mAh cm}^{-2}$).

at C-rates of 0.1, 0.2, 0.5, 1.0, 2.0, and 4.0 C, respectively, while showing a high average Coulombic efficiency of >99%. The corresponding electrochemical charging/discharging curves in Figure 6B validates the good rate performance of the cell under different C-rates between 2.7 and 4.4 V.

Due to its excellent Li-dendrite suppression capacity and stable CEI formation, the Li|CPE-PHCE|LNO cell retains 81% of capacity after 200 deep charge/discharge cycles with an average CE of >99.5% (Figure 6E). On the other hand, the capacity of LNO cell with CPE film drops quickly to almost zero with an CE always less than 90% due to the continual side reactions between lithium anode and CPE film, which induces large cell polarization and impedance increase, thus leading to fast capacity degradation (Figure S20). Further cycling of LNO cell with 2.0 mAh cm⁻² retains 81% of capacity with an average Coulombic efficiency of >99.6% after 150 deep cycles due to the formation of stable SEI and CEI (Figure S21). Compared with conventional and highly concentrated electrolytes (Figure S22), the design of CPE-PHCE is able to improve the CCD of CPE and enables a high-performance LNO cell via interface engineering: the LNO cell with CPE-PHCE is more stable than that with conventional electrolyte (38% of capacity retention after 120 cycles), and more practical than HCEs-based cell.

Please cite this article in press as: Deng et al., In situ formation of polymer-inorganic solid-electrolyte interphase for stable polymeric solid-state lithium-metal batteries, Chem (2021), https://doi.org/10.1016/j.chempr.2021.06.019





Conclusions

In summary, we systematically studied the interfacial issues between PVDF-based CPEs and Li metal due to insufficient surface contact, chemical/electrochemical instability and Li-dendrite growth. To address these challenges, a new design of CPE-PHCE film was proposed by building a thin, salt-rich interlayer using rapid UV polymerization. It was found that the CPE-PHCE membrane presents enhanced ionic conductivity of 1.2 \times 10⁻⁴ S/cm, a high Li⁺ transference number of 0.67, and high oxidation stability of >5.0 V. Lithium dendrites can be suppressed as demonstrated in the cycling of symmetric Li cells by presenting a high CCD of \sim 4.5 mA cm⁻² and Coulombic efficiency of >99%. Extensive characterizations show that the formation of polymeric-inorganic and LiF-rich SEI are key to suppressing Li dendrites and reducing dead-lithium accumulation in cycling. Finally, the SSLB based on a Cofree, LiNiO₂ composite cathode exhibited excellent electrochemical performance of high-capacity retention (81% of initial capacity after 200 cycles), rate performance, and high average Coulombic efficiency of >99.8%. The present work proposes a novel and reliable method to make CPEs suitable for high-energy Li-metal batteries coupling with Ni-rich cathodes and thus paves the way to commercialization of quasi-solid or solid-state lithium batteries.

EXPERIMENTAL PROCEDURES

Resource availability

Lead contact

Further information and requests for resources and reagents should be directed to and will be fulfilled by the lead contact, Chunsheng Wang (cswang@umd.edu).

Materials availability

This study did not generate new unique reagents.

Data and code availability

All data needed to support the conclusions of this manuscript are included in the main text or the supplemental information.

Fabrication of composite polymer electrolyte

The LLZTO garnet electrolyte was synthesized via conventional solid-state reaction technique. ^{9,22} To avoid the formation of passivation layer, the prepared microsized LLZTO powder was stored in the Ar glovebox for further usage. LiTFSI (>99.0%, Sigma-Aldrich) and PVDF powder (Arkema, Kynar 761) were dried at 120°C under vacuum for 24 h to remove moisture.

All the fabrication processes, including materials dry, polymer electrolytes preparation and battery assembling, were in Ar-filled glovebox with $\rm H_2O$ content <0.1 ppm to avoid the moisture in air. The preparation of PVDF-based CPEs was based on previously reported solution-casting method. ^{16,33} PVDF, LiTFSI, and LLZTO (6:2:1 by weight ratio) were first dissolved in DMF solvent with a polymer concentration of 15 wt %, followed by mechanical stirring with conditioning mixer (2,000 rpm/min) for 1 h to obtain a homogeneous solution. After that, the homogenized mixture was cast with a doctor blade on a clean and flat PTFE plate. Finally, the solid composite electrolyte membranes were obtained by further drying in vacuum oven at 70° C for 24 h to remove the trace of the DMF solvent.

Fabrication of PEGMA-LiFSI-FEC gel electrolytes

Polymer solutions, including BEMA (Sigma-Aldrich, $M_n = 1,700$), PEGMA (Sigma-Aldrich, $M_n = 500$), and 2-Hydroxy-2-methylpropiophenone (HMPP, Sigma-Aldrich,





Table 1. Detailed weight ratio for each component in the CPE-PHCE precursor solution with optimized high ionic conductivity and good film-forming capability

Components	LiFSI	PEGMA	BEMA	HMPP	FEC
Weight ratio (%)	43.75%	28.86%	3.17%	0.72%	23.6%

 $\rm M_w$ = 164.2) were drought using molecular sieves before use. The rapid-photopolymerization of PEGMA-based gel polymer electrolytes has been reported and studied by previous works. 37,48,49

Specifically, the CPE-PHCE and LiNiO $_2$ composite cathode were prepared by *in situ* photo-polymerization of precursor solution on the prepared CPEs and LiNiO $_2$ cathode (LiNiO $_2$: PVDF: carbon black = 8:1:1), respectively. To enhance the ionic conductivity and the film-forming capability, a specific amount of FEC (Sigma-Aldrich, 99%) is applied as plasticizer. The optimized precursor solution is obtained by mixing the as-blended monomers with LiFSI (SAFT, 99.9%) together (Table 1). To form a thin and uniform top layer, some specific amount of precursor solution was dropped on the CPEs, followed by casting and extruding with quartz glasses. After that, the CPE fixed by quartz glasses was photopolymerized with UV-lamp for \sim 20 s under Ar gas condition. The prepared CPE-PHCE membrane would be cut into disks and stored in Ar-filled glovebox for use.

The ratio of PEGMA, LiFSI, and FEC should be in isotropic phase range without phase separation. An optimal composition of different monomers or components for the precursor polymer solution has been shown in Table 1.

Synthesis of cobalt-free LiNiO₂ cathode

The synthesis of microsized LiNiO $_2$ cathode via simple sintering has been reported before. ³² Specially, the Ni(OH) $_2$ microparticles (Sigma-Aldrich) and LiOH·H $_2$ O powder (Sigma-Aldrich) were mixed with a molar ratio of 1.01:1 Li/Ni in mortar and calcined at 650°C for 12 h (ramp rate: 5°C min $^{-1}$) under an O $_2$ atmosphere. After sintering, the as-prepared LiNiO $_2$ microparticles were quickly transferred into Ar glovebox for further use.

Material characterizations

SEM and high-resolution TEM images in present work were taken at the University of Maryland using Hitachi SU-70 analytical GEG SEM (Japan) and JEOL JEM (Japan) 2100 LaB6 transmission electron microscope with an electron accelerating voltage of 200 KeV, respectively. Depth profiles of CPE-PHCE film was analyzed using ToF-SIMS attached to a ${\rm Ga^+}$ focused-ion beam (FIB)/SEM (Tescan GAIA3) at an accelerated voltage of 20 kV and 1 nA current. FTIR was recorded by NEXUS 670 FTIR instrument. $^1{\rm H}$ -spectra (104.63 MHz) were recorded on a Bruker 500 AVANCE spectrometer at University of Maryland. The corresponding samples were dissolved in d^6 -dimethyl sulfoxide (d^6 -DMSO) and measured at RT, while the signals were referenced to d^6 -DMSO (2.5 ppm for $^1{\rm H}$).

The Powder XRD data were collected with a Bruker D8 X-ray diffractometer using Cu K α radiation (λ = 1.5418 Å). XPS data were collected using a high-sensitivity X-ray photoelectron spectrometer (Kratos AXIS 165, Mg K α radiation) at the University of Maryland. The CasaXPS software was utilizing to fitting the XPS spectra to distinguish different species, and C1s peak (284.8 eV) was used as the reference to calibrate binding energy values. The thermogravimetry (TG) analysis was performed with Ar flowing over the samples heated at a rate of 2°C min⁻¹ with a TGA-DSC

Please cite this article in press as: Deng et al., *In situ* formation of polymer-inorganic solid-electrolyte interphase for stable polymeric solid-state lithium-metal batteries, Chem (2021), https://doi.org/10.1016/j.chempr.2021.06.019





instrument (Cahn TG2131). Raman measurements were performed on a Horiba Jobin Yvon Labram Aramis using a 532 nm diode-pumped solid-state laser.

AFM nanoindentation: mechanical analysis on the CPE/CPE-PHCE films was performed using a commercial AFM system (Cypher ES Environmental AFM, Asylum Research, USA). The nanomechanical property of the polymer film was mapped via the AM-FM (amplitude modulation–frequency modulation) Viscoelastic Mapping Mode using a diamond coated silicon AFM probe with a spring constant around 180 N m⁻¹ N and a resonant frequency of about 500 kHz. Before all characterization, the inverse optical lever sensitivity of the cantilever was calibrated using thermal noise methods. The elastic modulus of the polymer film was determined by fitting the force-separation curves with the Hertz model.

Electrochemical measurements

The prepared CPE-PHCE film electrolytes were cut into disks with diameter of 5/8 inch. The thickness of the CPE-PHCE membrane was measured and controlled to 80–100 μm . All cell assembly/disassembly (coin cell CR2032) was performed in an Ar-filled glove box with moisture and O_2 contents below 0.1 ppm. Ionic conductivities of CPE and designed CPE-PHCE film at different temperatures (30°C–80°C) were determined by EIS over a frequency range of 1.0 MHz to 0.1 Hz on an Auto Lab workstation using SS|CPE|SS or SS|CPE-PHCE|SS coin cells (SS, stainless steel electrodes). Ionic conductivities were calculated by the equation below:

$$\sigma = \frac{L}{R * S}$$
 (Equation 1)

where L is thickness of the CPE/CPE-PHCE, R presents the resistance value of the bulk electrolyte and S stands for the effective contacting area between the electrolyte and SS electrodes. Transference number t_{+} was calculated by the following equation:

$$t_{+} = \frac{I_{s}(\Delta V - I_{0}R_{0})}{I_{0}(\Delta V - I_{s}R_{s})}$$
 (Equation 2)

where ΔV is the voltage polarization applied, Is and Rs are the steady state current and resistance, respectively, IO and RO are the initial current and resistance, respectively. Applied voltage polarization for polymer electrolytes was 50 or 100 mV.

The cyclic voltammogram of the Li|CPE-PHCE|SS and Li|CPE|SS cells were tested with a scan rate of 2.0 mV s⁻¹ on a CHI 600E electrochemical workstation (CH Instruments USA). Interfacial stability of Li-electrolyte was conducted in the symmetric cell (Li|CPE-PHCE|Li, Li|CPE|Li), as well as Li|CPE-PHCE(CPE)|Cu cells. Electrochemical performances of the symmetric cell and the solid-state batteries (Li|CPE-PHCE|LiNiO₂) were investigated on Neware BTS-610 instrument with the voltage window of 2.7–4.4 V at RT. The current density here was calculated based on the LiNiO₂ mass in the composite electrode, 1 C = 200 mA g⁻¹). Lithium foil (20- μ m thick Li-metal on Cu foil) with areal capacity of 4 mAh cm⁻² is used as the anode. The areal mass loading of LiNiO₂ cathode is around 4–5 mg cm⁻², corresponding to areal capacity of 0.8–1.0 mAh cm⁻² and N/P ratio of 4:1 in capacity for the full cell.

SUPPLEMENTAL INFORMATION

Supplemental information can be found online at https://doi.org/10.1016/j.chempr. 2021.06.019.





ACKNOWLEDGMENTS

This work was supported by the Energy Efficiency and Renewable Energy Office of the U.S. Department of Energy through the Battery 500 Consortium Seedling project under contract no. DEEE0008202. T. Deng is grateful for the financial support of Battery 500 Young Investigators Awards. The authors gratefully acknowledge the support of the Maryland NanoCenter and its AIM Lab.

AUTHOR CONTRIBUTIONS

T.D. and C.W. proposed the research and designed the experiment. T.D., L.C., X.H., A.-M.L., D.L., J.X., S.L., P.B., T.J., L.M., M.A.S., and X.F. performed the experiments (material synthesis/preparation, characterizations, battery fabrication and testing, etc.). L.C. and S.L. performed SEM and TEM analysis. X.H. conducted the AFM analysis. T.D. and C.W. analyzed the data and wrote the manuscript with suggestions and comments from all of the authors.

DECLARATION OF INTERESTS

The authors declare no competing interests.

Received: February 1, 2021 Revised: March 5, 2021 Accepted: June 18, 2021 Published: October 14, 2021

REFERENCES

- Xu, W., Wang, J., Ding, F., Chen, X., Nasybulin, E., Zhang, Y., and Zhang, J.-G. (2014). Lithium metal anodes for rechargeable batteries. Energy Environ. Sci. 7, 513–537.
- 2. Liu, B., Zhang, J.-G., and Xu, W. (2018). Advancing lithium metal batteries. Joule *2*, 833–845.
- 3. Lin, D., Liu, Y., and Cui, Y. (2017). Reviving the lithium metal anode for high-energy batteries. Nat. Nanotechnol. 12, 194–206.
- 4. Manthiram, A., Yu, X., and Wang, S. (2017). Lithium battery chemistries enabled by solidstate electrolytes. Nat. Rev. Mater. 2, 1–16.
- Famprikis, T., Canepa, P., Dawson, J.A., Islam, M.S., and Masquelier, C. (2019). Fundamentals of inorganic solid-state electrolytes for batteries. Nat. Mater. 18, 1278–1291.
- 6. Kato, Y., Hori, S., Saito, T., Suzuki, K., Hirayama, M., Mitsui, A., Yonemura, M., Iba, H., and Kanno, R. (2016). High-power all-solid-state batteries using sulfide superionic conductors. Nat. Energy 1, 1–7.
- Ohta, S., Kobayashi, T., Seki, J., and Asaoka, T. (2012). Electrochemical performance of an allsolid-state lithium ion battery with garnet-type oxide electrolyte. J. Power Sources 202, 332–335.
- Liu, B., Gong, Y., Fu, K., Han, X., Yao, Y., Pastel, G., Yang, C., Xie, H., Wachsman, E.D., and Hu, L. (2017). Garnet solid electrolyte protected Limetal batteries. ACS Appl. Mater. Interfaces 9, 18809–18815.
- 9. Murugan, R., Thangadurai, V., and Weppner, W. (2007). Fast lithium ion conduction in

- garnet-type $Li_7La_3Zr_2O_{12}$. Angew. Chem. Int. Ed. Engl. 46, 7778–7781.
- Knauth, P. (2009). Inorganic solid Li ion conductors: an overview. Solid State Ionics 180, 911–916.
- Ortiz, G.F., López, M.C., Lavela, P., Vidal-Abarca, C., and Tirado, J.L. (2014). Improved lithium-ion transport in NASICON-type lithium titanium phosphate by calcium and iron doping. Solid State Ionics 262, 573–577.
- Manuel Stephan, A.M., and Nahm, K.S. (2006). Review on composite polymer electrolytes for lithium batteries. Polymer 47, 5952–5964.
- Manuel Stephan, A.M. (2006). Review on gel polymer electrolytes for lithium batteries. Eur. Polym. J. 42, 21–42.
- Liu, W., Lee, S.W., Lin, D., Shi, F., Wang, S., Sendek, A.D., and Cui, Y. (2017). Enhancing ionic conductivity in composite polymer electrolytes with well-aligned ceramic nanowires. Nat. Energy 2, 1–7.
- Quartarone, E., Mustarelli, P., and Magistris, A. (1998). PEO-based composite polymer electrolytes. Solid State Ionics 110, 1–14.
- Yao, P., Zhu, B., Zhai, H., Liao, X., Zhu, Y., Xu, W., Cheng, Q., Jayyosi, C., Li, Z., Zhu, J., et al. (2018). PVDF/Palygorskite nanowire composite electrolyte for 4 V rechargeable lithium batteries with high energy density. Nano Lett 18, 6113–6120.
- Park, C. (2003). Electrochemical stability and conductivity enhancement of composite polymer electrolytes. Solid State Ionics 159, 111–119.

- Chen, L., Li, Y., Li, S.-P., Fan, L.-Z., Nan, C.-W., and Goodenough, J.B. (2018). PEO/garnet composite electrolytes for solid-state lithium batteries: from "ceramic-in-polymer" to "polymer-in-ceramic". Nano Energy 46, 176–184.
- Wan, J., Xie, J., Kong, X., Liu, Z., Liu, K., Shi, F., Pei, A., Chen, H., Chen, W., Chen, J., et al. (2019). Ultrathin, flexible, solid polymer composite electrolyte enabled with aligned nanoporous host for lithium batteries. Nat. Nanotechnol. 14, 705–711.
- Wang, X., Zhang, Y., Zhang, X., Liu, T., Lin, Y.H., Li, L., Shen, Y., and Nan, C.W. (2018). Lithiumsalt-rich PEO/Li_{0.3}La_{0.557}TiO₃ interpenetrating composite electrolyte with three-dimensional ceramic nano-backbone for all-solid-state lithium-ion batteries. ACS Appl. Mater. Interfaces 10, 24791–24798.
- Li, Z., Zhang, H., Sun, X., and Yang, Y. (2020). Mitigating interfacial instability in polymer electrolyte-based solid-state lithium metal batteries with 4 V cathodes. ACS Energy Lett 5, 3244–3253.
- 22. Deng, T., Ji, X., Zhao, Y., Cao, L., Li, S., Hwang, S., Luo, C., Wang, P., Jia, H., Fan, X., et al. (2020). Tuning the anode–electrolyte interface chemistry for garnet-based solid-state Li metal batteries. Adv. Mater. 32, e2000030.
- 23. Taylor, N.J., Stangeland-Molo, S., Haslam, C.G., Sharafi, A., Thompson, T., Wang, M., Garcia-Mendez, R., and Sakamoto, J. (2018). Demonstration of high current densities and extended cycling in the garnet Li₇La₃Zr₂O₁₂ solid electrolyte. J. Power Sources 396, 314–318.

Chem Article



- Han, F., Yue, J., Zhu, X., and Wang, C. (2018). Suppressing Li dendrite formation in Li₂S-P₂S₅ solid electrolyte by Lil incorporation. Adv. Energy Mater 8, 1703644.
- Fan, X., Ji, X., Han, F., Yue, J., Chen, J., Chen, L., Deng, T., Jiang, J., and Wang, C. (2018). Fluorinated solid electrolyte interphase enables highly reversible solid-state Li-metal battery. Sci. Adv. 4, eaau9245.
- Liang, J.Y., Zeng, X.X., Zhang, X.D., Wang, P.F., Ma, J.Y., Yin, Y.X., Wu, X.W., Guo, Y.G., and Wan, L.J. (2018). Mitigating interfacial potential drop of cathode-solid electrolyte via ionic conductor layer to enhance interface dynamics for solid batteries. J. Am. Chem. Soc. 140, 6767–6770.
- Ebadi, M., Marchiori, C., Mindemark, J., Brandell, D., and Araujo, C.M. (2019). Assessing structure and stability of polymer/lithium-metal interfaces from first-principles calculations.
 J. Mater. Chem. A 7, 8394–8404.
- 28. Wu, N., Li, Y., Dolocan, A., Li, W., Xu, H., Xu, B., Grundish, N.S., Cui, Z., Jin, H., and Goodenough, J.B. (2020). In situ formation of Li₃P layer enables fast Li⁺ conduction across Li/solid polymer electrolyte interface. Adv. Funct. Mater. *30*, 2000831.
- 29. Liu, S., Imanishi, N., Zhang, T., Hirano, A., Takeda, Y., Yamamoto, O., and Yang, J. (2010). Effect of nano-silica filler in polymer electrolyte on Li dendrite formation in Li/poly (ethylene oxide)–Li (CF₃SO₂)₂N/Li. J. Power Sources 195, 6847–6853.
- Suo, L., Xue, W., Gobet, M., Greenbaum, S.G., Wang, C., Chen, Y., Yang, W., Li, Y., and Li, J. (2018). Fluorine-donating electrolytes enable highly reversible 5-V-class Li-metal batteries. Proc. Natl. Acad. Sci. USA 115, 1156–1161.
- Fan, X., Chen, L., Ji, X., Deng, T., Hou, S., Chen, J., Zheng, J., Wang, F., Jiang, J., Xu, K., and Wang, C. (2018). Highly fluorinated interphases enable high-voltage Li-metal batteries. Chem 4, 174–185.
- Deng, T., Fan, X., Cao, L., Chen, J., Hou, S., Ji, X., Chen, L., Li, S., Zhou, X., Hu, E., et al. (2019). Designing in-situ-formed interphases enables highly reversible cobalt-free LiNiO₂ cathode

- for Li-ion and Li-metal batteries. Joule *3*, 2550–2564.
- 33. Zhang, X., Liu, T., Zhang, S., Huang, X., Xu, B., Lin, Y., Xu, B., Li, L., Nan, C.W., and Shen, Y. (2017). Synergistic coupling between Li_{6.75}La₃Zr_{1.75}Ta_{0.25}O₁₂ and poly (vinylidene fluoride) induces high ionic conductivity, mechanical strength, and thermal stability of solid composite electrolytes. J. Am. Chem. Soc. 139, 13779–13785.
- Liu, W., Liu, N., Sun, J., Hsu, P.C., Li, Y., Lee, H.W., and Cui, Y. (2015). Ionic conductivity enhancement of polymer electrolytes with ceramic nanowire fillers. Nano Lett 15, 2740– 2745.
- Zhao, C.Z., Zhang, X.Q., Cheng, X.B., Zhang, R., Xu, R., Chen, P.Y., Peng, H.J., Huang, J.Q., and Zhang, Q. (2017). An anion-immobilized composite electrolyte for dendrite-free lithium metal anodes. Proc. Natl. Acad. Sci. USA 114, 11069–11074.
- 36. Suo, L., Borodin, O., Gao, T., Olguin, M., Ho, J., Fan, X., Luo, C., Wang, C., and Xu, K. (2015). "Water-in-salt" electrolyte enables highvoltage aqueous lithium-ion chemistries. Science 350, 938–943.
- Kim, H.-S., Kum, K.-S., Cho, W.-I., Cho, B.-W., and Rhee, H.-W. (2003). Electrochemical and physical properties of composite polymer electrolyte of poly (methyl methacrylate) and poly (ethylene glycol diacrylate). J. Power Sources 124, 221–224.
- Zhang, M., Zhang, A.-Q., Zhu, B.-K., Du, C.-H., and Xu, Y.-Y. (2008). Polymorphism in porous poly (vinylidene fluoride) membranes formed via immersion precipitation process. J. Membr. Sci. 319, 169–175.
- Janakiraman, S., Surendran, A., Ghosh, S., Anandhan, S., and Venimadhav, A. (2016). Electroactive poly (vinylidene fluoride) fluoride separator for sodium ion battery with high Coulombic efficiency. Solid State Ionics 292, 130–135.
- Weinhold, S., Litt, M.H., and Lando, J.B. (1980). The crystal structure of the γ phase of poly (vinylidene fluoride). Macromolecules 13, 1178–1183.

- 41. Cai, X., Lei, T., Sun, D., and Lin, L. (2017). A critical analysis of the α , β and γ phases in poly (vinylidene fluoride) using FTIR. RSC Adv 7, 15382–15389.
- Zheng, Y., Yao, Y., Ou, J., Li, M., Luo, D., Dou, H., Li, Z., Amine, K., Yu, A., and Chen, Z. (2020). A review of composite solid-state electrolytes for lithium batteries: fundamentals, key materials and advanced structures. Chem. Soc. Rev. 49, 8790–8839.
- Dixit, M.B., Zaman, W., Hortance, N., Vujic, S., Harkey, B., Shen, F., Tsai, W.-Y., De Andrade, V., Chen, X.C., Balke, N., and Hatzell, K.B. (2020). Nanoscale mapping of extrinsic interfaces in hybrid solid electrolytes. Joule 4, 207–221.
- Dixit, M.B., Regala, M., Shen, F., Xiao, X., and Hatzell, K.B. (2019). Tortuosity effects in garnettype Li₇La₃Zr₂O₁₂ solid electrolytes. ACS Appl. Mater. Interfaces 11, 2022–2030.
- Chen, J., Fan, X., Li, Q., Yang, H., Khoshi, M.R., Xu, Y., Hwang, S., Chen, L., Ji, X., Yang, C., et al. (2020). Electrolyte design for LiF-rich solid– electrolyte interfaces to enable highperformance microsized alloy anodes for batteries. Nat. Energy 5, 386–397.
- Tikekar, M.D., Choudhury, S., Tu, Z., and Archer, L.A. (2016). Design principles for electrolytes and interfaces for stable lithiummetal batteries. Nat. Energy 1, 16114.
- Choudhury, S., and Archer, L.A. (2016). Lithium fluoride additives for stable cycling of lithium batteries at high current densities. Adv. Electron. Mater. 2, 1500246.
- Nair, J.R., Gerbaldi, C., Destro, M., Bongiovanni, R., and Penazzi, N. (2011). Methacrylic-based solid polymer electrolyte membranes for lithium-based batteries by a rapid UV-curing process. React. Funct. Polym. 71, 409–416.
- Li, S., Chen, Y.-M., Liang, W., Shao, Y., Liu, K., Nikolov, Z., and Zhu, Y. (2018). A superionic conductive, electrochemically stable dual-salt polymer electrolyte. Joule 2, 1838–1856.

Supplemental information

In situ formation of polymer-inorganic solid-electrolyte interphase for stable polymeric solid-state lithium-metal batteries

Tao Deng, Longsheng Cao, Xinzi He, Ai-Min Li, Dan Li, Jijian Xu, Sufu Liu, Panxing Bai, Ting Jin, Lin Ma, Marshall A. Schroeder, Xiulin Fan, and Chunsheng Wang

Table S1 | Performance comparison of symmetric Li cells based on polymer electrolytes or CPEs at room temperature, including PEO, PAN, PVDF-HFP, PVDF-types, etc. Most of these polymer electrolytes are made by solution-casting methods. CE: Coulombic efficiency.

Polymer/Li salts	Filler	Thickness (µm)	Total ASR(Ω cm²)	Ionic conductivity (mS/cm)	Stability (mA/cm²//h)	Li CE (%)	Solvent uptake* (%)
PEO-LiTFSI ¹	LLZTO particle	30	25	0.011	0.2//800 (60°C)	N/A	N/A
PEO-LiTFSI ²	LiZr ₂ (PO ₄) ₃	200	375	0.12	0.3//100 (40°C)	N/A	N/A
PEO-LiTFSI ³	Ti ₃ C ₂ T _x MXene	150	N/A	0.022	0.3//175 (60°C)	N/A	N/A
PAN-LiTFSI ⁴	SiO ₂ nanoparticle	110±10	257	0.085	0.2//200 (60°C)	N/A	N/A
PVDF- HFP/LiTFSI ⁵	LLZO nanofiber	N/A	220	0.95	0.5//150	N/A	10
PVDF-LiFSI ⁶	N/A	90	~300	0.118	0.5//80	94	15
PVDF/LiClO ₄ ⁷	Palygorskite nanowire	100	~330	0.12	0.15//60	N/A	23.6
PVDF/LiClO ₄ ⁸	LLZTO particle	100	N/A	0.5	0.3//40	N/A	13
Poly- DOL/LiTFSI ⁹	N/A	N/A	900	1.0	1.0//200	98	N/A
CPE-PHCE (this work)	LLZTO particle	90±10	160	0.12	1.0//440	>99	~7*

^{*-}Solvent uptake is estimated by the weight loss of TGA curves at 200°C.

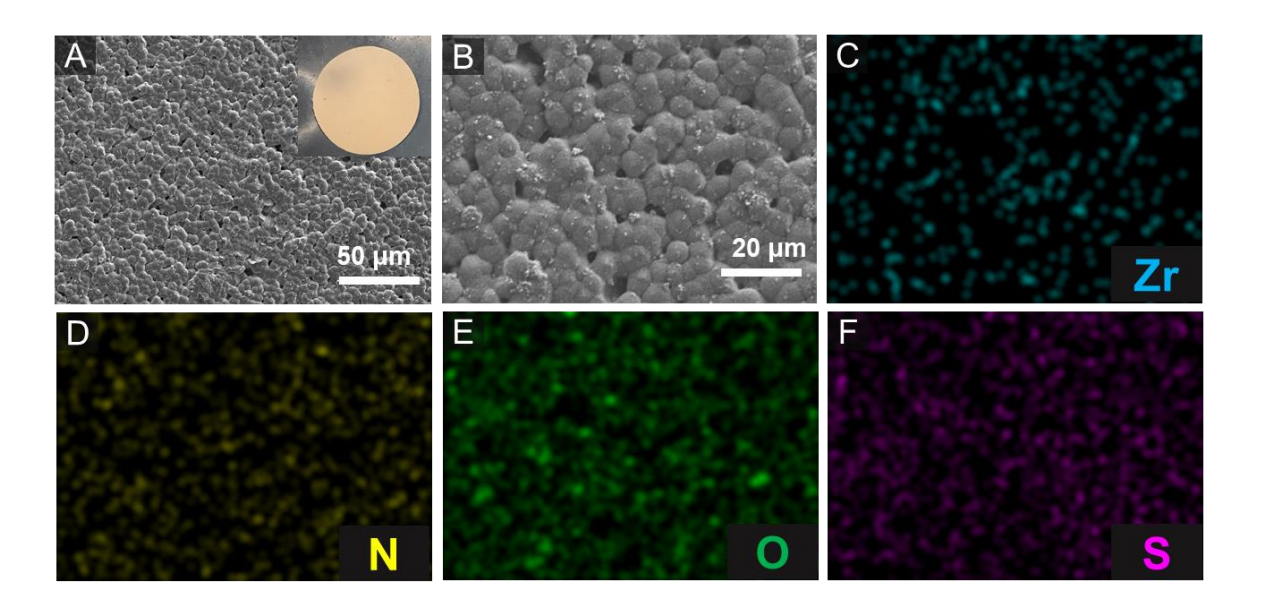


Figure S1 | **SEM Charaterization of as-prepared PVDF-CPEs**. **(A)** top surface of the CPE, which present nonhomogeneous surface with porous structure. **(B)** Typical SEM images of CPE for EDS mapping. **(C-F)** The elemental distributions of Zr, N, O and S, demonstrating the uniform dispersion of garnet filler and lithium salts on the surface.

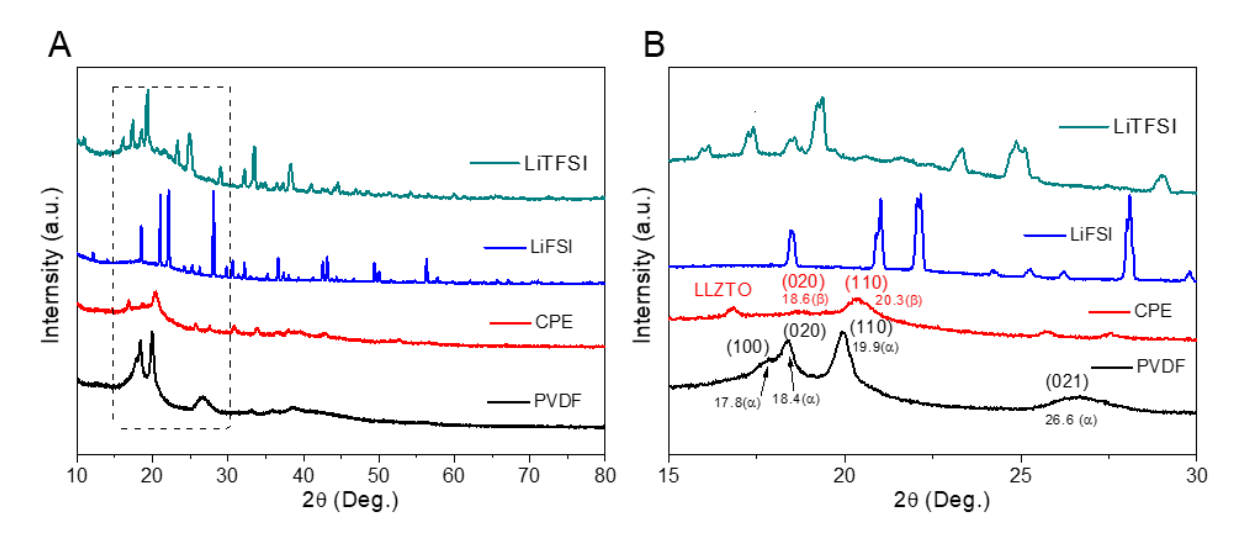


Figure S2 | **Phase analysis of CPE film.** (**A**) XRD patterns of LiTFSI, LiFSI, CPE and PVDF samples. (**B**) The enlarged view of the XRD pattern marked in (**A**), and the shifting of (020) and (110) indicates the transformation of α-phase to γ-phase for PVDF film electrolyte.

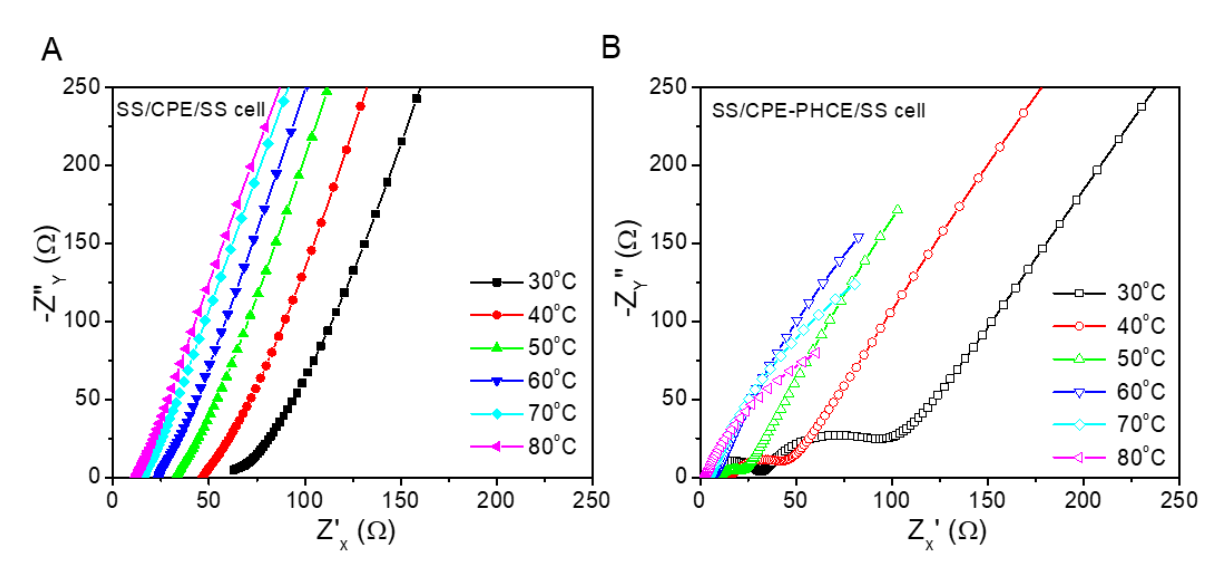


Figure S3 | Charaterication of the ionic conductivity of CPE and CPE-PHCE by measuring the electrochemical impedance spectroscopy curves of metal blocking cells. EIS curves of the (A) SS|CPE|SS cell and (B) SS|CPE-PHCE|SS cells at different temperatures ranging from 30°C to 80 °C, SS: stainless steel blocking electrode.

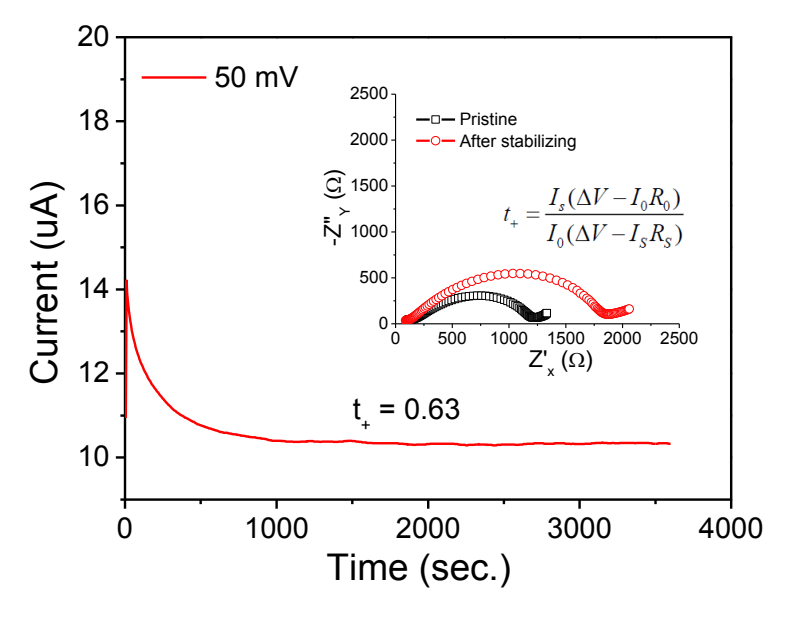


Figure S4 | Current-time profile of Li|CPE|Li symmetric cell after applying a DC voltage of 50 mV for determining Li⁺ transfer number. The inset shows the Nyquist impedance spectra of the cell before and after polarization.

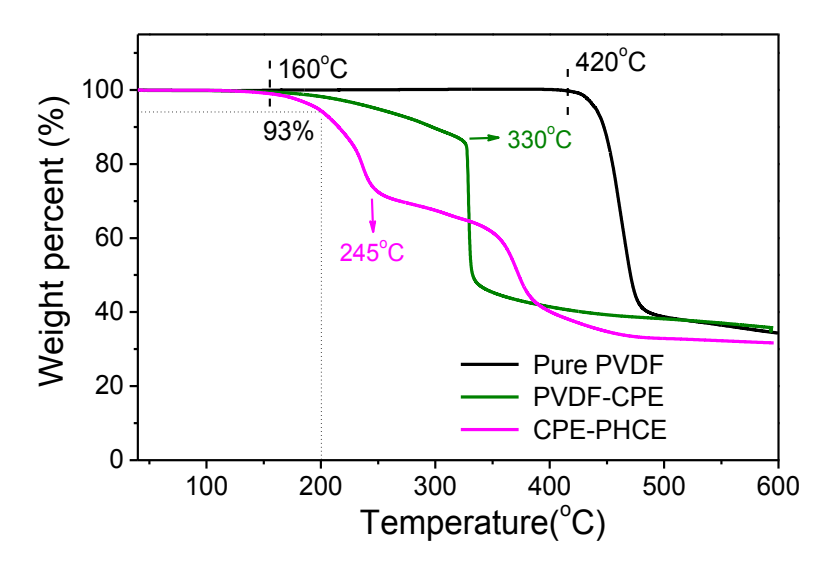


Figure S5 | Thermogravimetric analysis curves of CPE-PHCE membrane, CPE membrane and pure PVDF powder under Ar gas flow.

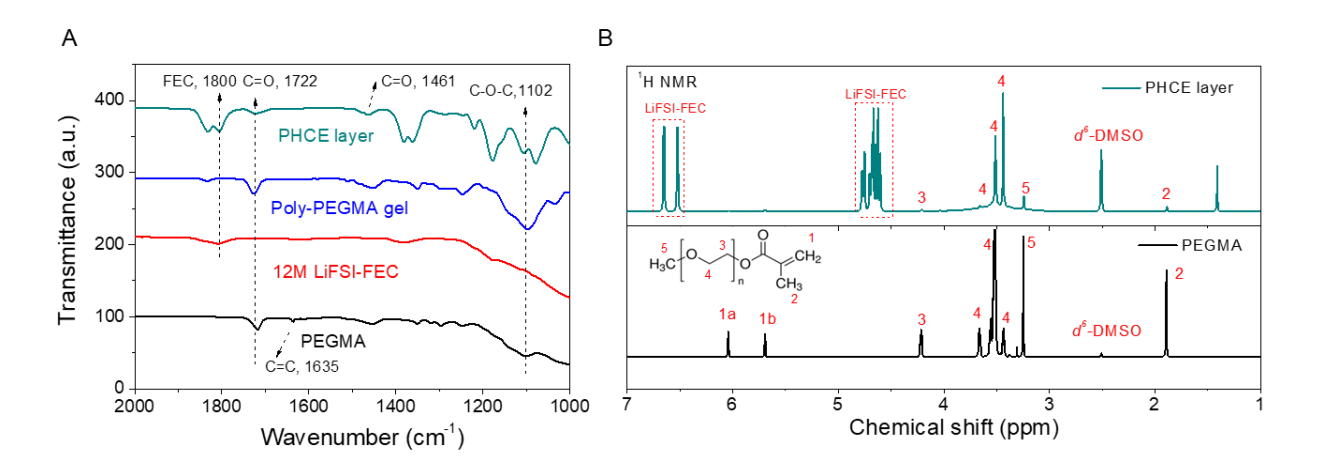


Figure S6 | **Additional characterization for the different components of CPE-PHCE.** (**A**) FTIR spectra of PHCE layer, Poly-PEGMA membrane, 12M LiFSI-FEC and PEGMA liquid. (**B**) ¹H NMR spectra of PHCE layer and PEGMEA liquid. The solvents are deuterated DMSO solvent. The inset shows the corresponding structural formula of PEGMA.

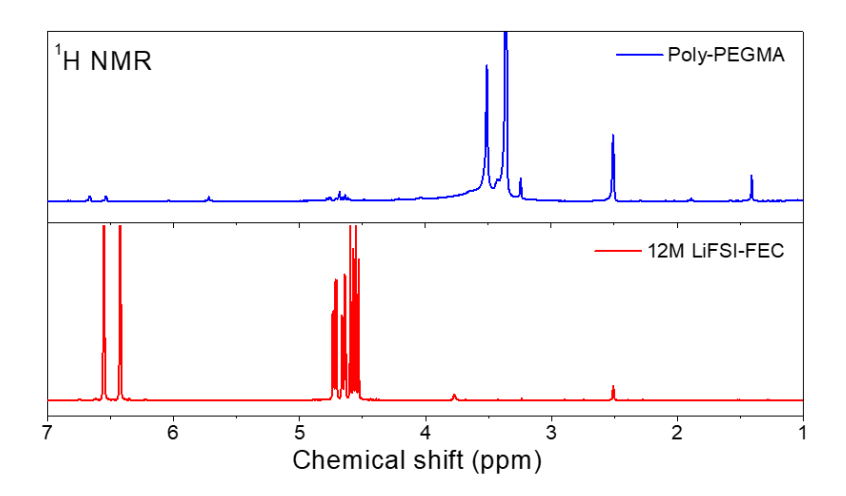


Figure S7 | ¹H NMR spectra of poly-PEGMA layer and 12M LiFSI-FEC electrolyte. The solvents used are deuterated DMSO.

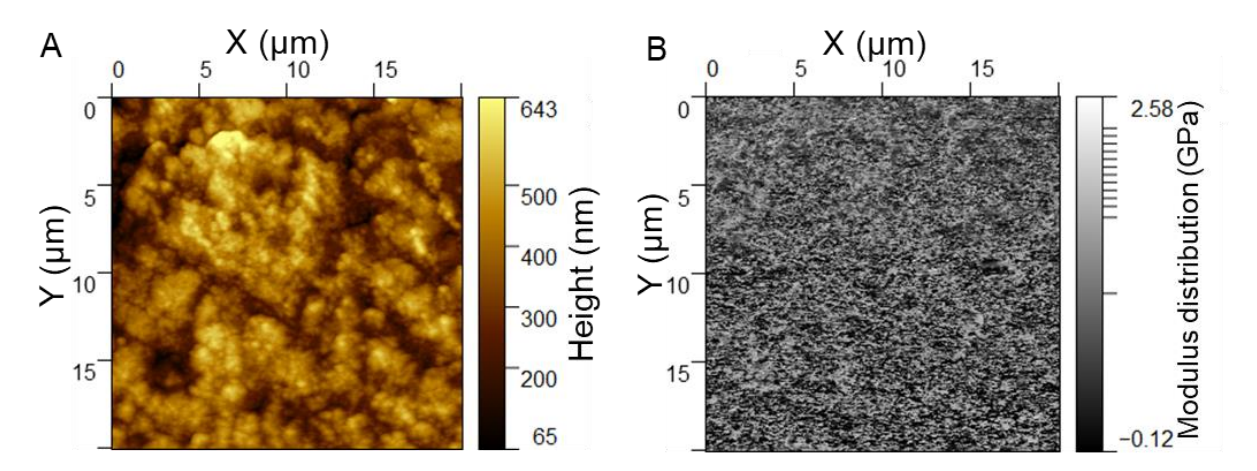


Figure S8 | AFM charaterization of CPE film. (A) AFM images (20 μ m x 20 μ m) of CPE film electrolytes with large surface roughness (~400 nm). (B) AFM mapping of the effective elastic modulus of CPE film, showing nonuniform mechnical strength of the surface.

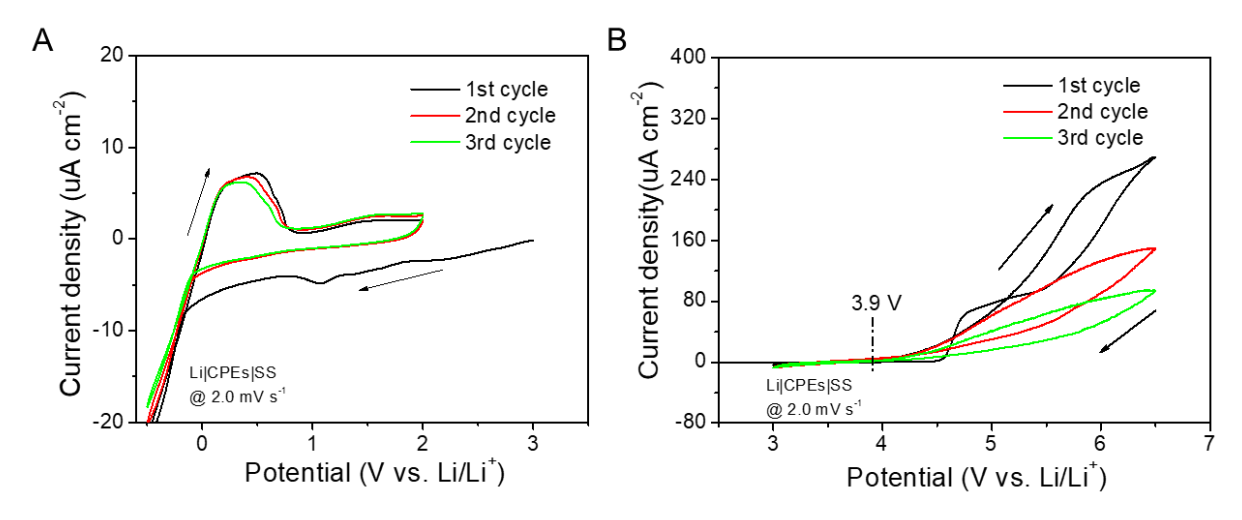


Figure S9 | Cyclic voltammetry curves of Li|CPE|SS cells from (A) -0.5-2.0 V and (B) 3.0-6.5 V. From -0.5V to 2.0 V, the cell presents voltage fluctuation due to continual side reaction beween CPE and Li metal and no SEI formation process can be observed. From 3.0 V to 6.5 V, the non-overlapping CV curves of the cell indicates the worse oxidation stability (~3.9 V) of the prepared CPE film. Scan rate: 2 mV s⁻¹.

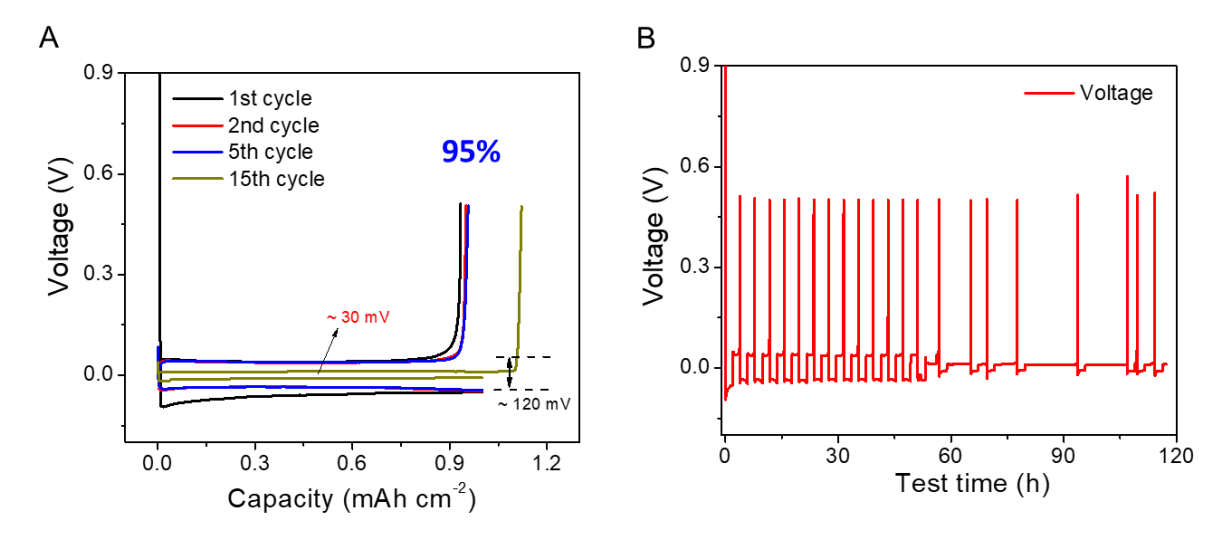


Figure S10 | **Stability of CPE film to Li metal.** (**A**) Li metal plating/stripping profiles of Li|CPE|Cu cell at a current density of 0.5 mA cm⁻² with areal capacity of 1.0 mAh cm⁻², and the polarization after stabilization is around 120 mV. (**B**) The corresponding voltage profile for Li plating/stripping CE after short within 120 h.

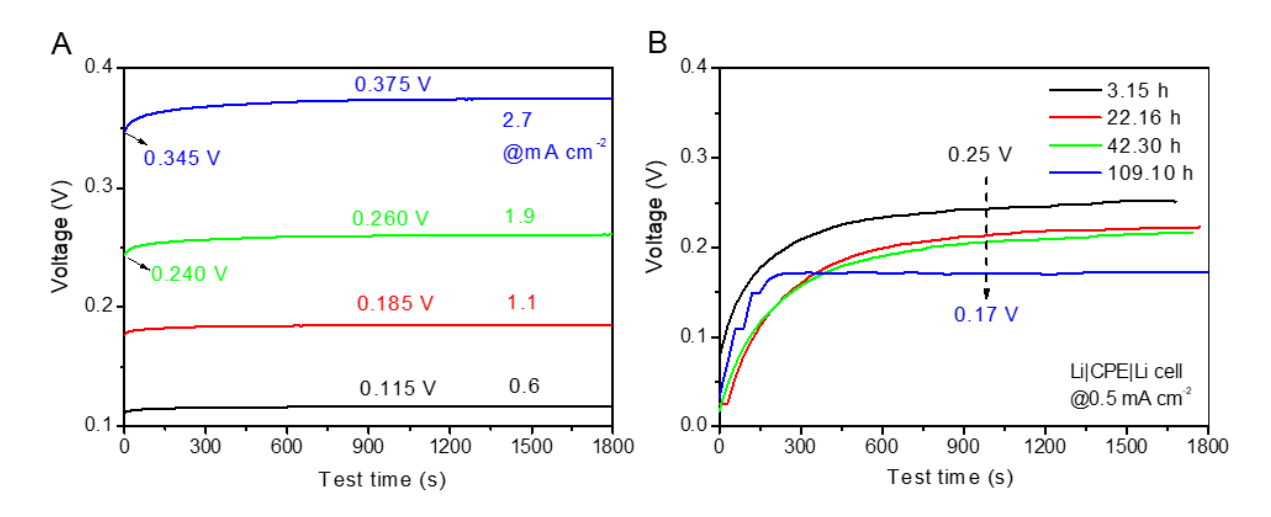


Figure S11. Voltage changes of Li plating for Li symmetric cells with (A) CPE-PHCE film in Figure 4c and (B) CPE film in Figure 4d.

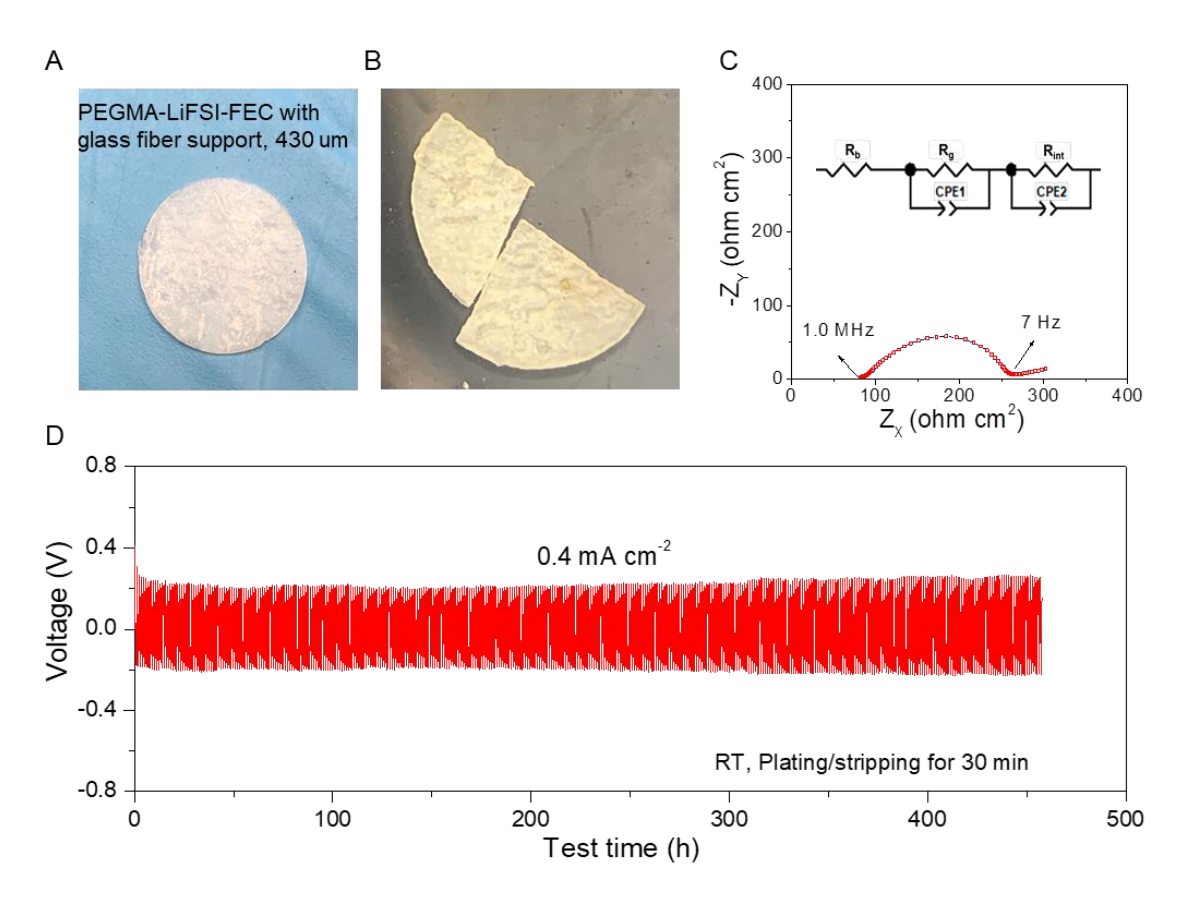


Figure S12 | **Charaterization of PHCE.** (a) Digital image of PEGMA-LiFSI-FEC film with glass fiber membrane support. (b) Cracked fragments of brittle PHCE-Glass fiber film. (c) Typical

Nyquist plot of Li symmetric cell based on the gel membrane, and the inset shows the equivalent circuit model for EIS fitting analysis. (d) Corresponding cycling of a symmetric Li cell with PHCE-glass fiber film at a current density of 0.4 mA cm^{-2} for > 450 h without short-circuit.

Since the resistance from grain boundary (R_g) of the polymer electrolytes is negligible, the intersection at high frequency stands for the bulk resistance (R_b) while the magnititude of semicicle represents the interface resistance (R_{int}). Based on the calculation, the ionic conductivity of prepared PEGMA gel film is around 4 x10⁻⁴ S/cm, which is about 4 times to that of CPE. The Li symmetric cell with PHCE-glass fiber support is able to stably cycle at 0.4 mA cm⁻² for more than 450 h without short-circuit, although the PHCE-glass fiber membrane is brittle and might be broken by high stacking pressure operation.

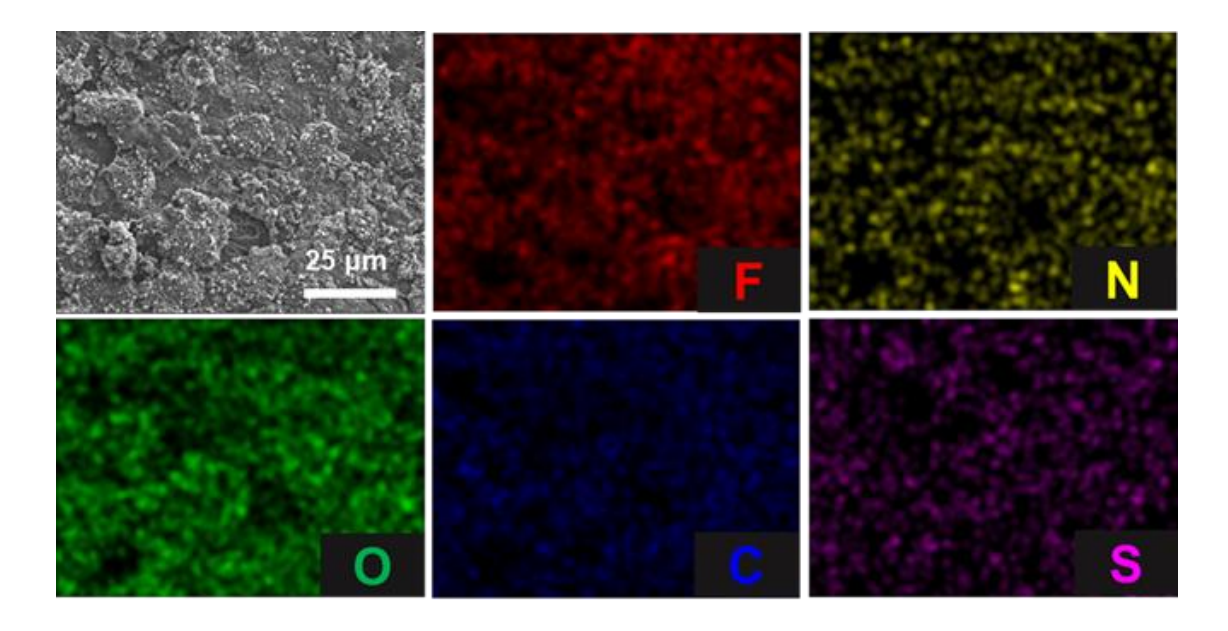


Figure S13 | SEM images of cycled Li metal harvested from Li|CPE-PHCE|Li cell for EDS mapping and the corresponding distribution of F, N, O, C and S elements. The cell was cycled at 0.5 mA cm⁻² for 50 h and cycled Li metal was cleaned with dimethyl ether solvent to remove absorbed Li salts or polymer.

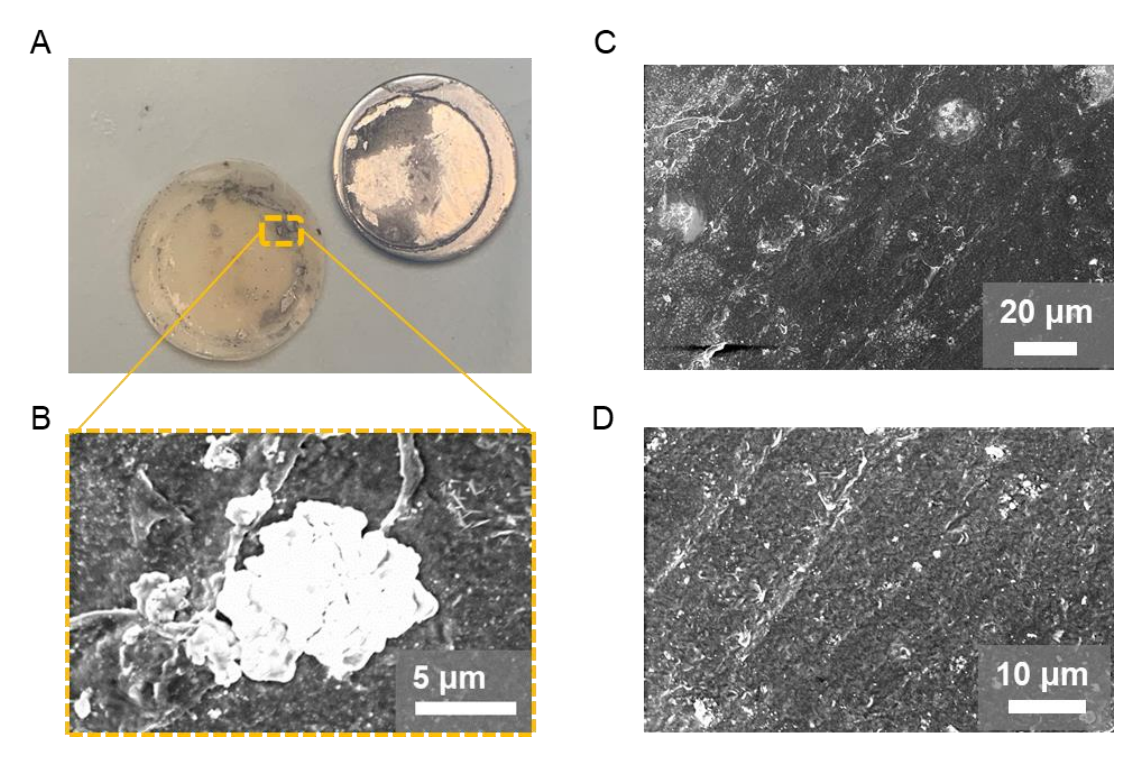


Figure S14 | Surface morphology of cycled & shorted CPE film obtained from a Li|CPE|Li cell after cycling at 0.2 mA cm⁻² for 200 h. (A) Digital image of cycled CPE film and Li metal with dead lithim on the top. (B) SEM image shows the recrystallized Li particles on CPE film due to Li dendrite penetration. (C, D) SEM images of cycled CPE film with different scales, showing the nonhomogeous morphology.

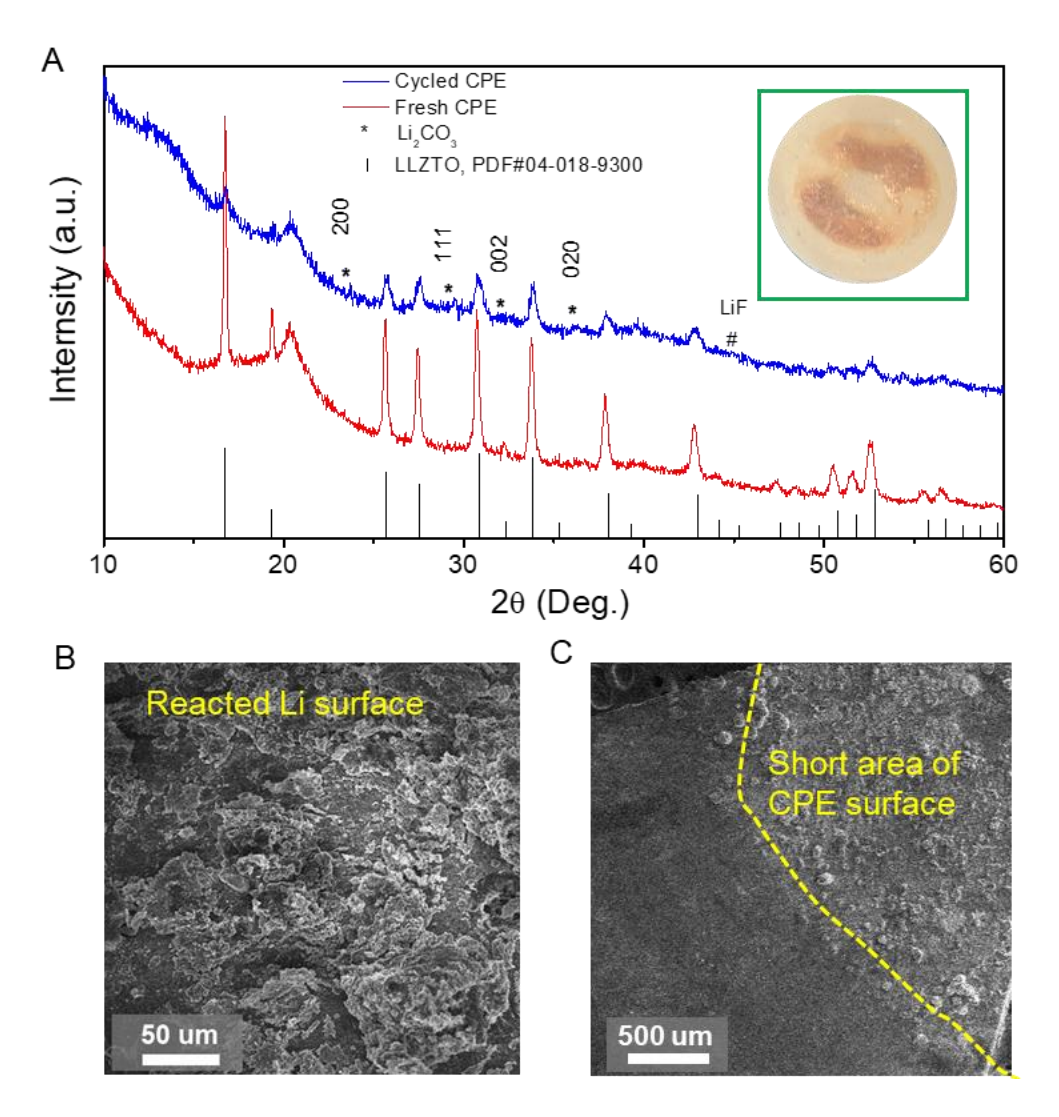


Figure S15 | **Post-morten charaterizaiton of shorted CPE cell.** (**A**) XRD patterns of pristine CPE and shorted CPE obtained from Li|CPE|Li cell at 0.5 mA cm⁻², indicating the decomposition of PVDF by Li metal after long cycling. (**B**) SEM image of the surface of cycled Li metal with decomposed products on the top. (**C**) SEM image of the shorted CPE showing the reacted surface by Li metal.

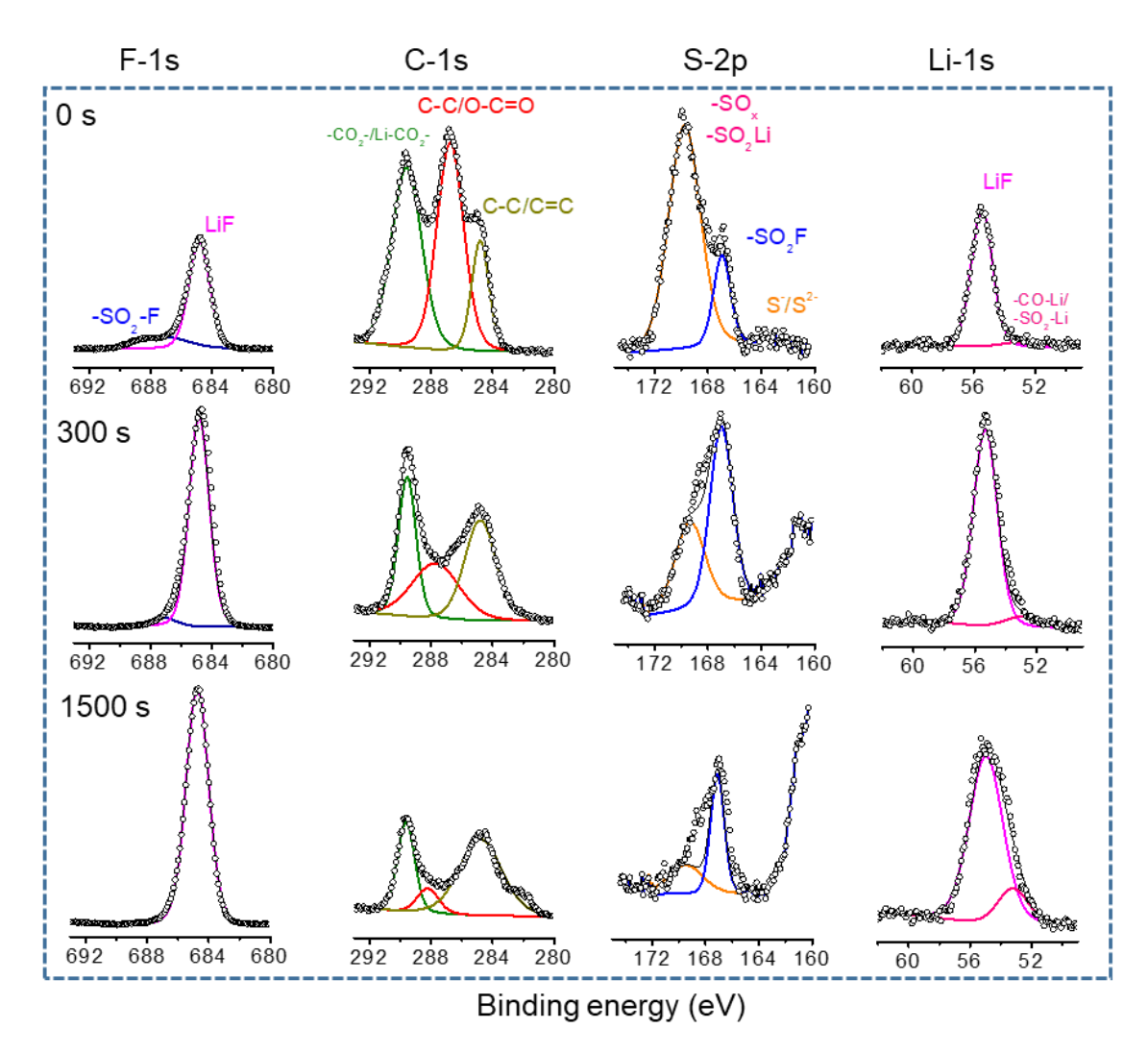


Figure S16 | XPS spectra of F-1s, C-1s, S-2p and Li-1s for cycled Li metal with CPE-PHCE film under different sputtering times of 0, 300, 1500 s. The Li metal was obtained from symmetric Li|CPE-PHCE|Li cell after cycling at 0.5 mA cm⁻² for 50 h at RT.

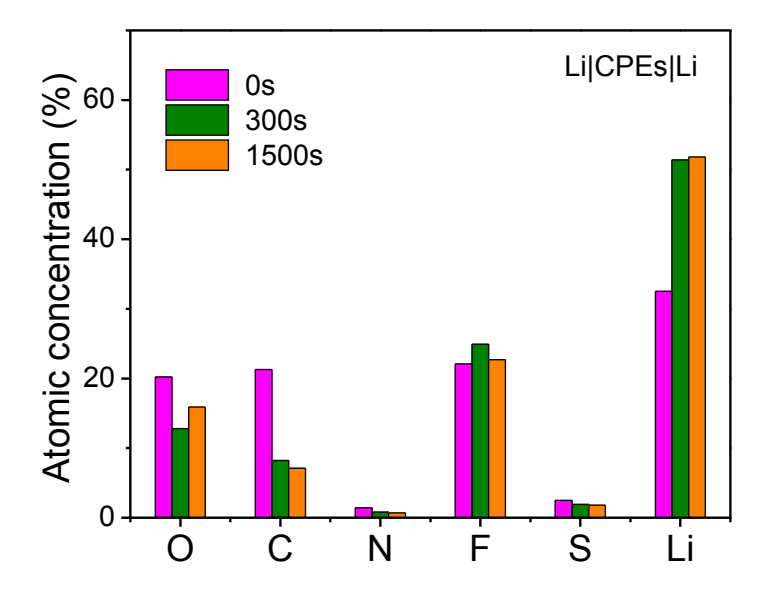


Figure S17 | XPS elemental concentration of the SEI on cycled Li metal with different sputtering times of 0, 300, 1500 s. The cycled Li metal was obtained from symmetric Li|CPE|Li cells after cycling at 0.5 mA cm⁻² for 50 h at RT.

Table S2 | Summary of bulk modulus, interface energy, band gap and electrochemical stability for some typical Li compounds based computational methods. 10-12

Li compounds	Bulk modulus (GPa)	Interface energy (meV/Ų)	DFT band gap (eV)	Electrochemical stability (vs. Li/Li ⁺)
LiF	70	73.28	8.9	0 - 6.3
Li ₂ O	78	38.70	4.7	0 - 2.9
Li ₂ CO ₃	63	59.22	5.0	N/A
Li ₂ S	40	19.01	3.5	0 - 2.0
LiCl	32	37.55	6.0	0 - 4.2
Li ₃ PS ₄	22	-88.92	N/A	1.7 - 2.3

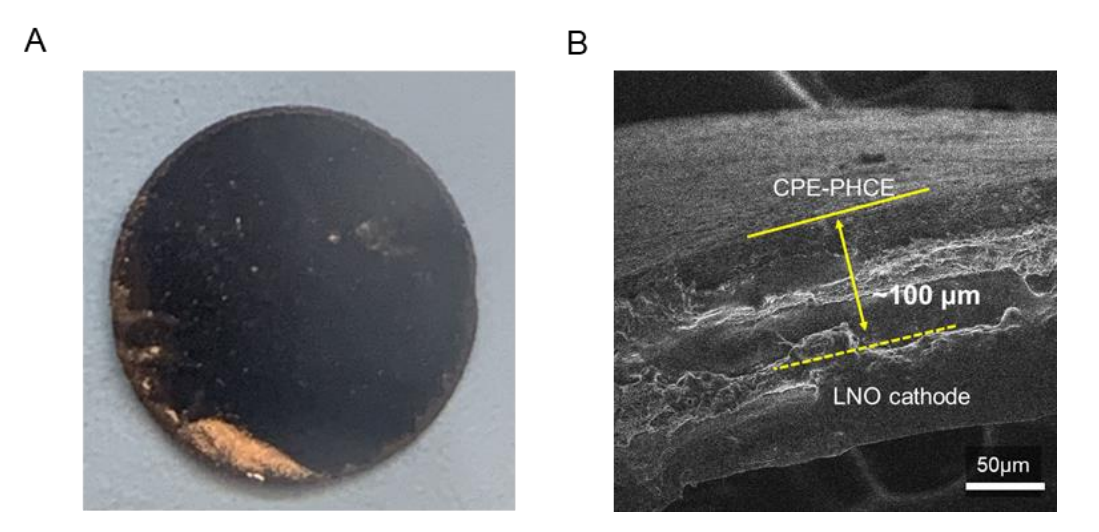


Figure S18 | **Design of LNO composite cathode.** (**A**) Image of the prepared LNO composite cathode by infusing the PEGMA-LiFSI-FEC precussor solution into LNO electrode followed by UV-cured process. (**B**) SEM image of cross section of CPE-PHCE|LNO interfaces, showing good contact between CPE-PHCE film and LNO composite cathode.

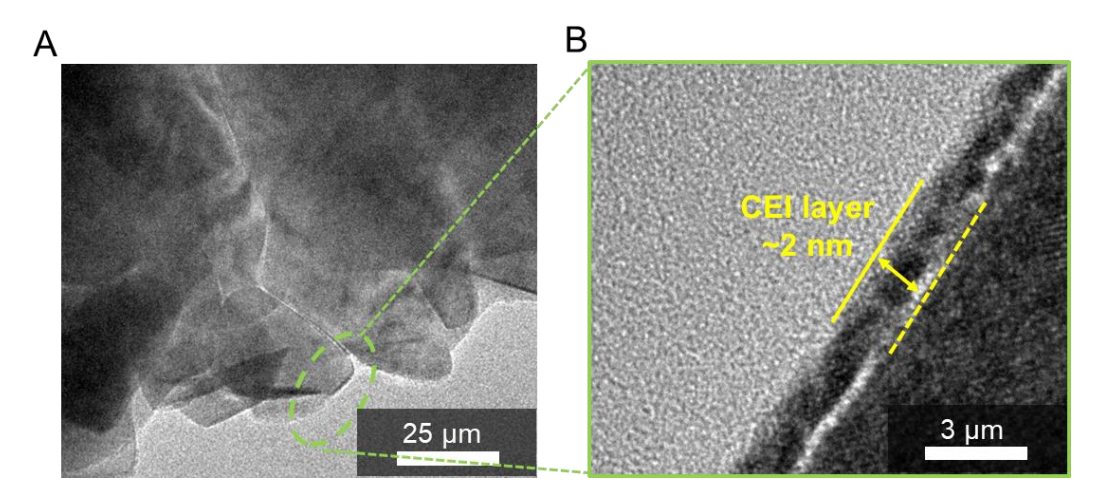


Figure S19 | **Charaterization of cycled LNO electrode.** (**A**) HRTEM image of LNO particle harvested from Li|CPE-PHCE|LNO cell after 200 cycles. (**B**) The enlarged view shows the formation a thin SEI layer on the surface of LNO with the thickness of ~2 nm, which protects the LNO from continual side reaction with the polymer.

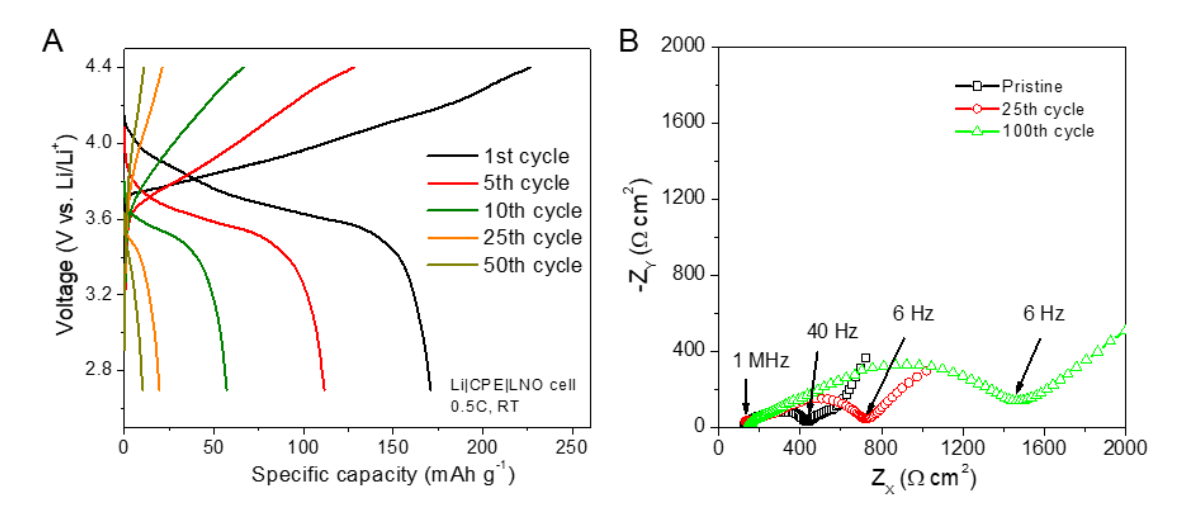


Figure S20 | **Electrochemical performance of Li**|CPE|LNO cell at RT. (A) Electrochemical charging/discharging curves of the LNO cell base on CPE film at a current density of 0.5 C. (B) Nyquist plots of the LNO cell at 0^{th} , 25^{th} , and 100^{th} cycles, showing the evolution of resistance during the testing (0.4 mA cm⁻², 1C = 200 mA g⁻¹).

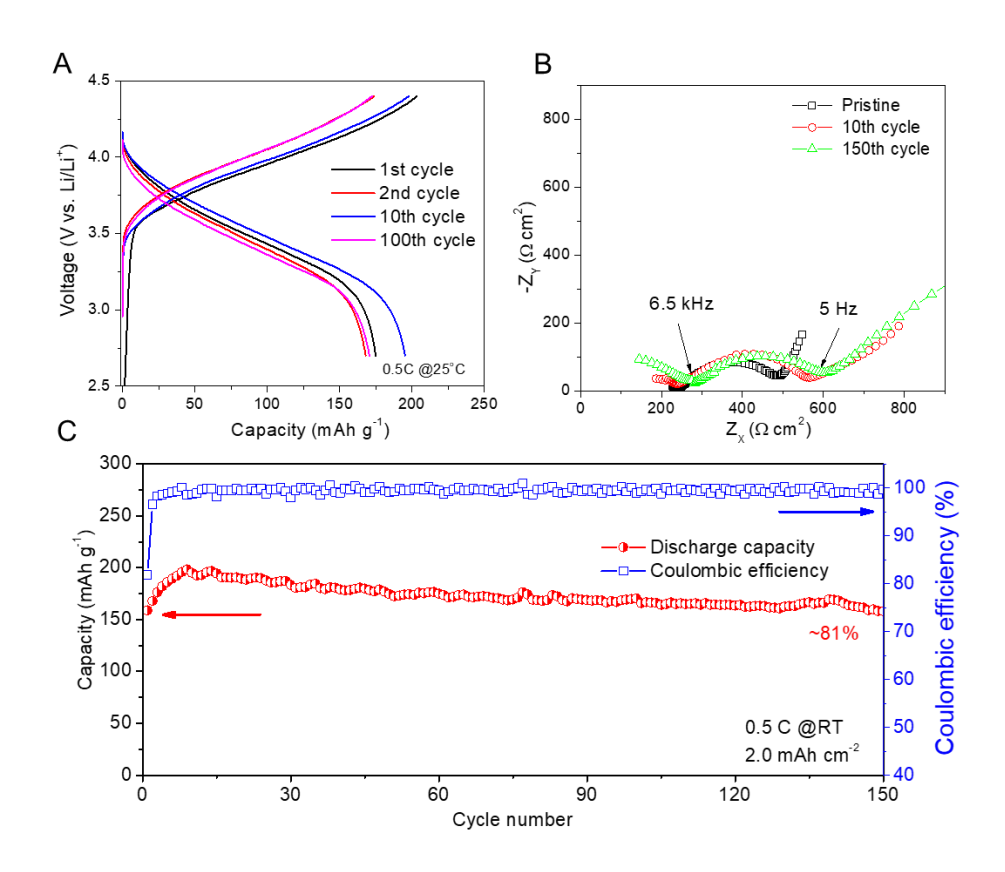


Figure S21 | Electrochemical performance of Li|CPE-PHCE|LNO cell with high loading at RT. (A) Electrochemical charging/discharging curves of the LNO cell at a current density of 0.5 C (\sim 1 mA cm⁻²). (B) Nyquist plots of the LNO cell at 0th, 10th, and 150th cycles, showing the evolution of resistance in cycling. (C) Corresponding cycling stability of LNO cell at constant current rate of 0.5 C, 1C = 200 mA g⁻¹, the areal capacity of composite cathode is \sim 2.0 mAh cm⁻².

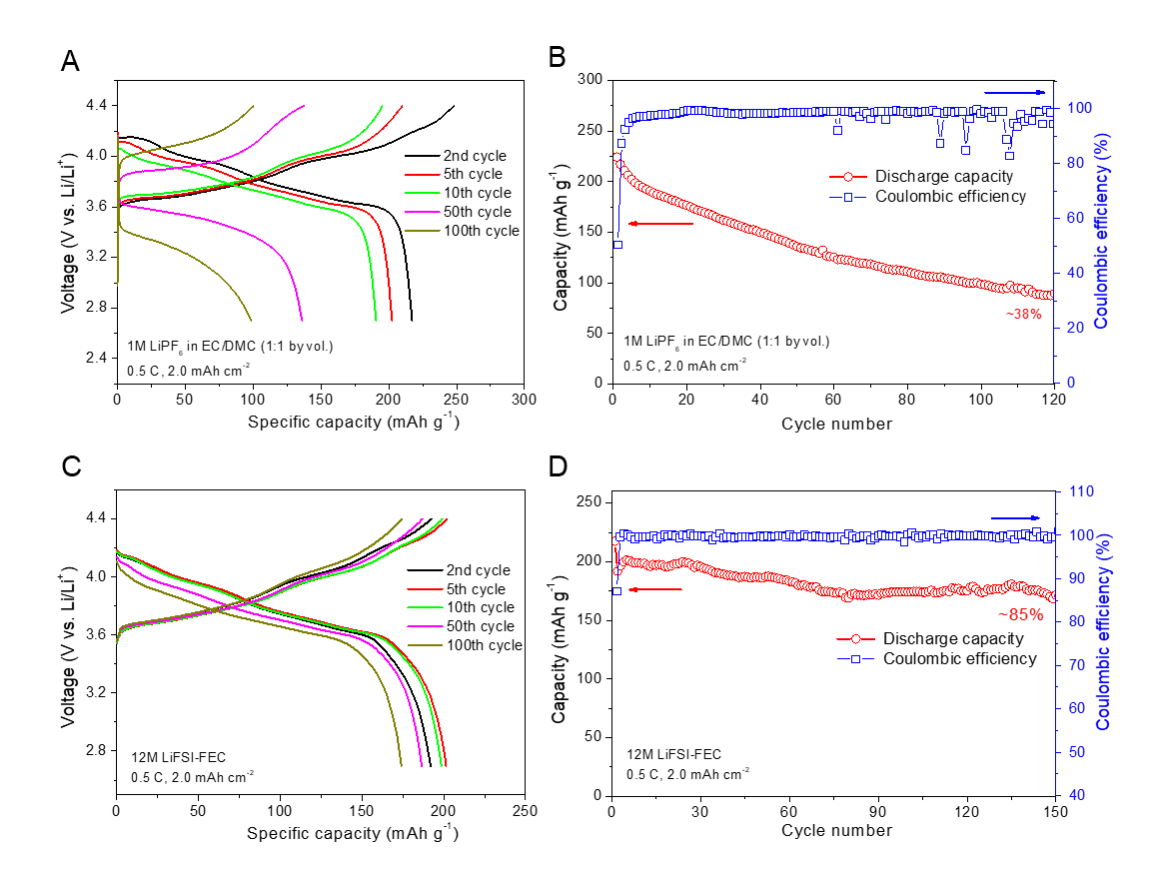


Figure S22 | Electrochemical performance of LiNiO₂ (LNO) cathode with different electrolytes at 0.5C (1 mA cm⁻²). (A, B) cycling performance of the LNO cell with conventional electrolyte-1M LiPF₆-EC/DMC (1:1 by vol.). (C, D) cycling performance of the LNO cell with highly concentrated electrolyte (12M LiFSI-FEC).

References

- (1) Zhao, C. Z.; Zhang, X. Q.; Cheng, X. B.; Zhang, R.; Xu, R.; Chen, P. Y.; Peng, H. J.; Huang, J. Q.; Zhang, Q. (2017). An anion-immobilized composite electrolyte for dendrite-free lithium metal anodes. *Proc. Natl. Acad. Sci. 114*, 11069-11074.
- (2) Wu, N.; Chien, P. H.; Li, Y.; Dolocan, A.; Xu, H.; Xu, B.; Grundish, N. S.; Jin, H.; Hu, Y. Y.; Goodenough, J. B. (2020). Fast Li⁺ Conduction Mechanism and Interfacial Chemistry of a NASICON/Polymer Composite Electrolyte. *J. Am. Chem. Soc.* 142, 2497-2505.
- (3) Pan, Q.; Zheng, Y.; Kota, S.; Huang, W.; Wang, S.; Qi, H.; Kim, S.; Tu, Y.; Barsoum, M. W.; Li, C. Y. (2019). 2D MXene-containing polymer electrolytes for all-solid-state lithium metal batteries. *Nanoscale Adv. 1*, 395-402.
- (4) Gao, H.; Grundish, N. S.; Zhao, Y.; Zhou, A.; Goodenough, J. B. (2021). Formation of Stable Interphase of Polymer-in-Salt Electrolyte in All-Solid-State Lithium Batteries. *Energy Mate. Adv. 2021*, 1-10.
- (5) Li, Y.; Zhang, W.; Dou, Q.; Wong, K. W.; Ng, K. M. (2019). Li₇La₃Zr₂O₁₂ ceramic nanofiber-incorporated composite polymer electrolytes for lithium metal batteries. *J. Mater. Chem. A.* 7, 3391-3398.
- (6) Zhang, X.; Wang, S.; Xue, C.; Xin, C.; Lin, Y.; Shen, Y.; Li, L.; Nan, C. W. (2019). Self-Suppression of Lithium Dendrite in All-Solid-State Lithium Metal Batteries with Poly(vinylidene difluoride)-Based Solid Electrolytes. *Adv. Mater.* 31, e1806082.
- (7) Yao, P.; Zhu, B.; Zhai, H.; Liao, X.; Zhu, Y.; Xu, W.; Cheng, Q.; Jayyosi, C.; Li, Z.; Zhu, J.; Myers, K. M.; Chen, X.; Yang, Y. (2018). PVDF/Palygorskite Nanowire Composite Electrolyte for 4 V Rechargeable Lithium Batteries with High Energy Density. *Nano Lett.* 18, 6113-6120.
- (8) Zhang, X.; Liu, T.; Zhang, S.; Huang, X.; Xu, B.; Lin, Y.; Xu, B.; Li, L.; Nan, C.-W.; Shen, Y. (2017). Synergistic coupling between Li_{6.75}La₃Zr_{1.75}Ta_{0.25}O₁₂ and poly (vinylidene fluoride) induces high ionic conductivity, mechanical strength, and thermal stability of solid composite electrolytes. *J. Am. Chem. Soc. 139*, 13779-13785.
- (9) Zhao, Q.; Liu, X.; Stalin, S.; Khan, K.; Archer, L. A. (2019). Solid-state polymer electrolytes with in-built fast interfacial transport for secondary lithium batteries. *Nat. Energy* 4, 365-373.
- (10) Fan, X.; Ji, X.; Han, F.; Yue, J.; Chen, J.; Chen, L.; Deng, T.; Jiang, J.; Wang, C. (2018). Fluorinated solid electrolyte interphase enables highly reversible solid-state Li metal battery. *Sci. Adv. 4*, eaau9245, 2375-2548.
- (11) Zhu, Y.; He, X.; Mo, Y. (2015). Origin of Outstanding Stability in the Lithium Solid Electrolyte Materials: Insights from Thermodynamic Analyses Based on First-Principles Calculations. *ACS Appl. Mater. Interfaces* 7, 23685-23693.
- (12) Chen, Y.; Ouyang, C.; Song, L.; Sun, Z. (2011). Electrical and lithium ion dynamics in three main components of solid electrolyte interphase from density functional theory study. *J. Phys. Chem. C. 115*, 7044-7049.